UNIVERSITY OF TARTU
FACULTY OF SCIENCE AND TECHNOLOGY
Institute of Chemistry

Kenneth Tuul

Ball-milled $NaAlH_4$/carbon black composites for reversible hydrogen storage

Master's thesis (30 ECTS)
Materials Science and Technology

Supervisor: Rasmus Palm, PhD

Tartu 2021

Ball milled $NaAlH_4$/carbon black composites for reversible hydrogen storage

New efficient and economically feasible hydrogen storage technologies are among the key enabling technologies for transitioning to a hydrogen economy. Sodium aluminum hydride ($NaAlH_4$) is an extensively studied and promising complex metal hydride for hydrogen storage. Its thermodynamic properties, kinetic properties, and cyclability are insufficient for practical applications. These properties can be improved by nanostructuring. In this master's thesis, composites of varying mass% of $NaAlH_4$ and commercial mesoporous carbon black Vulcan XC72R are synthesized via ball milling. The extent of the improvement of the composites' reversible hydrogen storage properties is studied.

Keywords: hydrogen economy, solid-state hydrogen storage, complex metal hydrides, carbon black, ball milling

CERCS code: P400 Physical chemistry, T140 Energy research, T150 Material technology

Kuulveskis jahvatatud $NaAlH_4$/süsiniktahm komposiitmaterjalid vesiniku pöörduvaks salvestamiseks

Vesinikuenergeetikale üleminekuks on uued tõhusad ning majanduslikult tasuvad vesiniku salvestamise meetodid üheks võtmetehnoloogiaks. Naatriuumalumiiniumhüdriid ($NaAlH_4$) on üks enim uuritumaid ja paljulubavamaid kompleksmetallhüdriide pöörduvaks vesiniku salvestamiseks. Paraku on selle termodünaamilised ja kineetilised omadused ning tsükleeritavus rakendusteks ebapiisavad. Neid omadusi on võimalik parandada $NaAlH_4$ viimine nanoosakeste kujule. Antud magistritöö raames sünteesiti erinevate massprotsendilise sisaldusega $NaAlH_4$ ja kommertsiaalse mesopoorse süsiniktahma Vulcan XC72R komposiite kuuljahvatamise meetodil. Seejärel analüüsitakse sünteesitud komposiitide vesiniku salvestamise omaduste paranemist.

Märksõnad: vesinikuenergeetika, tahkel kujul vesiniku salvestamine, kompleksmetallhüdriidid, süsiniktahm, kuulveskis jahvatamine

CERCS kood: P400 Füüsikaline keemia, T140 Energeetika, T150 Materjalitehnoloogia

Table of Contents

INTRODUCTION

In March of 2021, 23 hydrogen project idea applications for a total worth of € 1.5 billion were submitted in Estonia alone. This was done to map out ideas in the process of preparing an IPCEI – Important Project for Common European Interest [1]. The EU has set out a hydrogen strategy as a critical building block towards a climate-neutral and zero pollution economy in 2050. In it is an investment agenda to incentivize transitioning to renewable energy and a hydrogen-based economy [2]. In this new hydrogen economy, the primary energy source will shift from fossil fuels to renewables such as wind and solar power. Hydrogen's role in this is to be an energy carrier, as it is a clean energy source with infinite supply. During overproduction, the excess energy can be stored into electrolyzed hydrogen to be used when and where necessary [2–4].

One of the key enabling technologies in transitioning to a hydrogen economy is an efficient and economically feasible method for hydrogen storage. The US Department of Energy (DoE) has set targets for the gravimetric energy density, volumetric energy density, and cost of a mobile storage system to be reached by 2025, which are 1.8 kWh kg^{-1}, 1.3 kWh L^{-1}, and 9 \$ kWh^{-1}, respectively [5,6]. The current industry standard for mobile applications is the carbon fiber reinforced 700 bar high-pressure tank, which respective properties are estimated at 1.4 kWh kg^{-1}, 0.8 kWh L^{-1}, and 15 \$ kWh^{-1}. However, the Toyota Mirai storage system is claimed to have reached 1.9 kWh kg^{-1} and 1.4 kWh L^{-1} [7]. Chemically binding hydrogen into solid-state hydrides offers potential energy densities of upwards of 1.8 kWh kg^{-1} and 2.6 kWh L^{-1}, without the inherent safety issues and energy losses associated with high-pressure storage [3]. However, there is much improvement to be made regarding materials development to reach the DoE targets. The ideal material would have high gravimetric and volumetric energy densities, fast and controllable kinetics, reversibility, low cost, and an operating temperature in the same range as a polymer electrolyte membrane (PEM) fuel cell (< 80 °C) [3,6,7].

In this work, composite materials are synthesized and characterized for reversible hydrogen storage. Sodium aluminum hydride ($NaAlH_4$) is one of the most extensively studied hydrogen storage materials that is composed of abundant elements and has previously shown promising results. The component of the composite is the commercial nanoparticulate carbon black Vulcan XC72R (Cabot, USA). The synthesis method utilized is ball milling, which is the most widely used method for nanostructuring – the principal method for improving a hydride's H_2 storage properties used in this work. With a series of different mass% of $NaAlH_4$/Vulcan composites and several high-pressure cycling experiments, the enhancement of the $NaAlH_4$

reversible H_2 storage properties is demonstrated. This is thanks to the comparatively simple and energetically low-demanding synthesis method of ball milling and the synergetic effect of the nanoscaffolding carbon black.

1 LITERATURE OVERVIEW

1.1 Chemical hydrogen storage

Although hydrogen is an excellent medium for energy storage with 3 times higher gravimetric energy density than gasoline - 33 kWh kg^{-1} compared to 11 kWh kg^{-1} - it suffers from poor volumetric density. The density of hydrogen gas at 25 ℃ and 1 bar is 0.0813 g L^{-1}, and that of liquid hydrogen at −253 ℃ is 71.3 g L^{-1}. This is compared to the density of gasoline at roughly 800 g L^{-1}. Liquid hydrogen has an energy density of 2.35 kWh $L^{-1,}$ and compressed hydrogen at 700 bar has approximately 1.6 kWh L^{-1}. It is worth noting that this does not account for energy losses during compression or liquefaction, resulting in even lower actual energy densities [8]. The ideal hydrogen storage material should have high volumetric and gravimetric hydrogen densities, low dehydrogenation temperature, moderate dehydrogenation pressure, low heat of formation, low heat dissipation during hydride formation, reversibility, limited energy loss during dehydrogenation/hydrogenation cycles, fast kinetics, high environmental stability, cyclability, low cost of recycling and infrastructure, and high safety [9]. Chemically binding hydrogen in solid-state hydrogen offers a potentially efficient and environmentally friendly solution [10,11].

1.1.1 Metal hydrides

Many metals and alloys form hydrides with hydrogen, providing a medium for solid-state hydrogen storage under moderate temperature and pressure. Metal hydrides have significantly higher energy densities than high pressure or liquid hydrogen storage methods. In addition, it is safer, as there are no high pressures nor cryogenic liquids involved in the storage process. Light metals that form high hydrogen-to-metal ratio compounds, such as Li, Be, Na, Mg, B, and Al, are the most interesting for applications, especially for mobile applications, with MgH_2, and LiH the most studied [9].

Early d- and f-block metals and alloys (e.g., TiFe, $LaNi_5$) form metallic bonds with hydrogen and offer reversible storage under moderate conditions but are expensive and with low gravimetric hydrogen densities (< 2 mass%). Alkali metals that form more ionic bonds like LiH and MgH_2 have higher gravimetric densities of hydrogen (12.7 and 7.7 mass% respectively) but are rather stable, with high decomposition temperatures and poor kinetics. This is a significant drawback for mobile applications, but they are applicable in heat storage in solar thermal power technology [8,9].

AlH_3 or alane has more covalent bonds, high hydrogen content (10 mass%), and relatively low dehydrogenation temperatures of around 150-200 °C, which can be improved with ball milling. However, extremely high pressures (7000 bar at room temperature) are required for hydrogenation of Al to AlH_3, which is nearly impossible in practical conditions [12].

1.1.2 Complex metal hydrides

One class of hydrides that offer potentially high gravimetric hydrogen densities is complex hydrides. They are salt-like materials in which hydrogen is covalently bound to a central complex anion. Especially interesting are complex metal hydrides containing lighter metals such as Li, Na, Mg, and Al. The most intensely studied complex systems are alanates $[AlH_4]^-$, borohydrides $[BH_4]^-$, and amides $[NH_2]^-$, as they have low density and a high hydrogen-to-metal atom ratio. Volumetric densities of 150 g L^{-1} and gravimetric content of 18 mass% can be reached with these systems [9,13].

Complex metal hydrides were considered unsuitable for reversible storage due to the high kinetic and thermodynamic barriers of decomposition. However, a breakthrough was achieved by Bogdanović and Schwickardi when they discovered that doping with transition metals considerably lowers the thermal stability of the material [14]. This makes the material reversible closer to feasible conditions and their application as reversible hydrogen storage materials under moderate conditions more viable. This spurred a large amount of research into the synthesis and properties of complex hydrides [13].

Borohydrides have the highest gravimetric densities (18 mass% for $LiBH_4$), and $NaBH_4$ is stable in air, making it easy to handle. Their high thermodynamic stability can be bypassed by producing hydrogen through a hydrolysis process, enabling hydrogen evolution at temperatures below 60 °C. The H_2 density of the end-system is increased, reaching 10.8 mass%, which is up from 10.6 mass%, but only half of that is from the hydride, leading to an increased potential for reversibility. Still, borohydrides suffer from engineering difficulties such as thermal management, catalyst durability, mist elimination, and the requirement to hydrogenate outside the storage system. Furthermore, upon decomposition, there is a competing reaction where diborane is formed, which damages the catalyst or membrane of a fuel cell [13,15,16]. In the case of amides, the borderline kinetics and hydrogen content of up to 5.5 mass% and 40 g L^{-1} are negated by similar problems: poor reversibility, degradation during cycling, and a competing formation of ammonia, that threatens the membrane of PEM fuel cells [17,18].

The advantages of alanates, such as $LiAlH_4$ and $NaAlH_4$, are the low price and abundance of the component compounds, low weight, nontoxicity, and that no volatile gases besides hydrogen are formed. Most alanates possess high gravimetric densities, but thermodynamic and kinetic barriers have inhibited their application [13].

1.1.2.1 Sodium aluminum hydride ($NaAlH_4$)

Sodium aluminum hydride or sodium alanate ($NaAlH_4$) is an extensively studied low-density material that could be used for reversible hydrogen storage. Although greatly enhanced by Ti-based catalysts, the total hydrogenation of NaH and Al phases back to $NaAlH_4$ is difficult to achieve [13]. The cause is either the spatial separation of the NaH and Al phase or the accumulation of Al into larger particles after repeated cycling. This leads to the inevitable degradation of hydrogen storage capacity during cycling [19]. Ball milling the cycled material into smaller particles helps with the regeneration of $NaAlH_4$, but the solution is only temporary, as Al again starts to form agglomerates [3,19]. That is why it is necessary to find new methods to improve the hydrogen storage properties of $NaAlH_4$ in addition to simple catalysis.

$NaAlH_4$ has a relatively high hydrogen content (7.4 mass%). Although a promising material, the main limiting factor is its high kinetic barrier, although high required temperatures and poor reversibility are also issues [13,19,20]. $NaAlH_4$ decomposes in three stages (Figure 1):

$$NaAlH_4(s) \rightarrow \frac{1}{3}Na_3AlH_6(s) + \frac{2}{3}Al(s) + H_2 \uparrow \quad \text{(I)}$$

$$\frac{1}{3}Na_3AlH_6(s) \rightarrow NaH(s) + \frac{1}{3}Al(s) + \frac{1}{2}H_2 \uparrow \quad \text{(II)}$$

$$NaH(s) \rightarrow Na(l) + \frac{1}{2}H_2 \uparrow \quad \text{(III)}$$

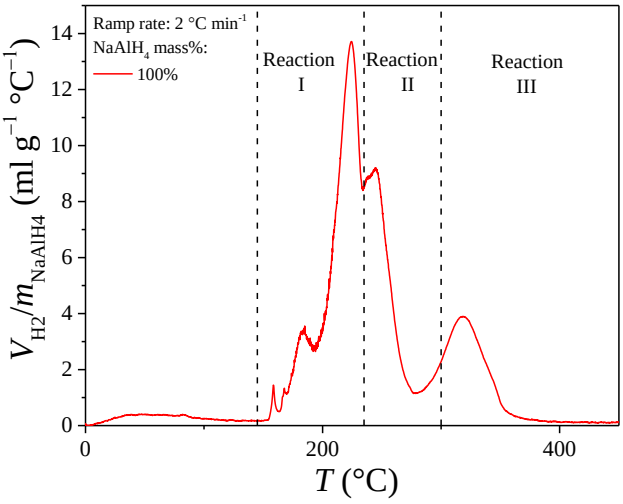

Figure 1. The differential volume of released hydrogen normalized with the mass of $NaAlH_4$.

The two first stages are reversible and release a total of 5.6 mass% of H_2, which is 75% of all H_2 in the material. The first stage is a prolonged process starting between 145-183 °C, where the kinetic hindrance is eliminated to a large degree upon reaching the melting point at 183°C. The second stage takes place around 240 °C, with the first and second stages overlapping and being indistinguishable in bulk alanate. The final, irreversible stage mainly occurs at temperatures >300 °C, as NaH is thermally very stable [3,13,20]. With catalysis and nanoscaling, significant improvements to kinetics, thermodynamics, and reversibility have been achieved, many of which are presented in chapter 1.3.2.

1.2 Porous scaffolding materials

Porous solid materials are classified into three categories according to size:

1) pores with widths > 50 nm are macropores,
2) pores with widths between 2 nm and 50 nm are mesopores,
3) pores with widths ≤ 2 nm are micropores,

with all pores ≤ 100 nm being classified as nanopores [21]. Porous materials have many important applications in catalysis, adsorption, molecular sieves, etc. Recent advances provide a wide range of materials with different and tunable properties, such as metal-organic frameworks (MOFs), covalent organic frameworks (COFs), or zeolites. They vary between crystalline and amorphous, stable and processable to unstable, etc. With this wide range of options, their choice and design become more and more function-driven [22].

Carbon materials are a preferred choice as scaffolding materials due to their low price, chemical inertness, high thermal stability in an inert atmosphere, low weight, and thermal conductivity. Carbons also may be surface-modified to enhance particle anchoring properties [23]. Especially of interest is their potential for high porosity, which leads to energy storage applications as hydrogen adsorbents, scaffolding for hydrides, and components in supercapacitors, batteries, and fuel cells. Porous carbons can be made from both biomass and synthetic sources, the latter offering more opportunities to fine-tune the final properties of the carbon material [24].

1.2.1 Carbon blacks

Carbon blacks are produced by the incomplete combustion of hydrocarbon fuel. Near spherical carbon nanoparticles are formed from aggregates of graphite nanocrystals. The size, shape, porosity, and specific surface area determine the physical properties of these materials. These nanoparticles are usually fused into larger aggregates due to van der Waals forces, which

themselves tend to agglomerate into larger particles. The final structure of carbon blacks is between graphitic and amorphous. Carbon blacks are used, for example, in the manufacture of rubber tires, inks and paints, polymers, and as catalyst support materials [25].

1.2.2 Vulcan XC72R

Vulcan XC72R (Cabot, USA) is a carbon black with low sulfur content used mainly as an additive in rubber and plastic applications [26]. In a previous study, Vulcan XC72R was extensively characterized [27]. In that study, it was found that the material consists of spherical particles in the range of 30 to 60 nm that have agglomerated into aggregates. Vulcan has a turbostratic structure, meaning it is between amorphous and graphitic. The specific surface area was found to be 218 $m^2\ g^{-1}$, with a total pore volume of 0.41 $cm^3\ g^{-1}$. The carbon black has a mesoporous structure, although a large number (30% of surface area) of micropores are also present. The material has been extensively used as electrocatalyst support in PEM fuel cells [27,28].

1.3 Nanoconfinement for hydrogen storage

Nanostructured materials that have at least one dimension on the nanoscale (1-100 nm) are known to have shown different physical and chemical properties compared to bulk materials [29,30]. Thermodynamic properties, e.g., melting and phase transition temperatures, are affected mainly by size and surface effects. Surface atoms have fewer neighbors and more unsatisfied bonds. Smaller particles have higher surface-to-volume ratios, and many properties follow this downscaling. In narrow pores, it has been shown that solubility, the melting point, and even the critical point of a fluid are greatly reduced. Phase transitions are collective phenomena, hence with fewer atoms, they are much less sharply defined. A small cluster of atoms behaves more similarly to a molecule than bulk materials, and different structural isomers may coexist over a range of temperatures [30].

There are many studies where nanoscaling effects and nanoconfinement have been used to improve the hydrogenation and dehydrogenation properties of hydrides. Nanoconfinement is a broad term, where most often the nanostructured material is in nanoparticle form, i.e., all three dimensions are on the nanoscale. Nanoconfinement is loosely divided into nanoscaffolding and nanoencapsulation. In nanoscaffolding, the material is confined inside a scaffold material with permanent nanoscale pores or recesses. The material is introduced, bound, and then restricted from movement or agglomeration with other particles, and the final

structure of the nanoscale material is determined by the scaffolding material. In nanoencapsulation, the nanomaterial is coated in a rigid matrix [29].

Significant effects on kinetics, thermodynamic properties, and stability over several hydrogenation/dehydrogenation cycles have been achieved. Particle size is the most appropriate property for predicting the effects of nanoscaling. Although exact values vary from material to material, it is desirable for particles to be ≤ 20 nm, with the most dramatic effects occurring when the critical dimension is ≤ 10 nm. However, it is unclear if or what is the crucial universal factor for any given system: surface-to-volume ratio, particle-host interaction, or cluster geometry, with size-independent effects from the scaffolding, also possibly present. The interpretation based on simply shorter diffusion times and lengths is appropriate but simplistic [29].

In addition to thermodynamic properties, which may be improved by increasing the surface-to-volume ratio, another issue that inhibits solid-state hydrogen storage applications is slow kinetics. When viewing the hydrogenation process, which is usually slower than dehydrogenation, five processes can be discerned: hydrogen physisorption at the surface, dissociation of the H_2 molecule or chemisorption, surface penetration by the hydrogen into the material, diffusion to the metal/hydride interface, and conversion of metal into hydride. It is generally expected that hydrides form preferably at a surface or interface rather than in the bulk of the material. The rate-limiting steps are usually either the dissociation of hydrogen or the diffusion of hydrogen through the hydride. Decreasing particle size deals with both of these issues by reducing the required diffusion distances in solid-state and increasing surface area and surface activity [23].

Nanoconfinement restricts phase segregation, which maintains particle size and is essential in complex systems, where the dehydrogenation/hydrogenation processes involve multiple phases (complex hydrides and mixed hydride systems, see chapter 1.1.2.1). When multiple phases are involved, the restriction of decomposition products negates the need for them to diffuse together in order to form a hydride forming interface during hydrogenation. Furthermore, confinement restricts denser phases from collecting at the bottom of a storage tank [23].

1.3.1 Role of scaffolding materials in nanoconfinement

Scaffolding materials have several vital roles in nanostructured systems. It facilitates the formation of very small particles, prevents sintering, and improves the overall properties and stability of the system. It is also suspected that the scaffold/nanomaterial interface influences

the properties of the latter. Although carbon is not considered active, its surface may be activated to improve the anchoring of nanoparticles. Furthermore, as in porous materials, the nanoparticles are restricted in 3D, and the dehydrogenation/hydrogenation process involves a change in volume, the boundary condition may affect the stability of the hydride. Finally, heat transport and mechanical stability of the system must be taken into consideration in real systems. Hence, the scaffolding should have good thermal conductivity to aid heat transfer and disperse the medium thoroughly to avoid, for example, blockages [23].

The decrease in the mass% of the active hydrogen storing phase and the increase of volume with the use of a scaffolding material are well compensated by the system's increased performance, i.e., the enhancement of the capability to store hydrogen reversibly. The most common method for impregnation of porous materials is solution impregnation, but melt-infiltration has also provided noteworthy results. Ball milling has been a major step forward regarding nanoscaling and remains the most widespread method for obtaining nanoparticles [23].

1.3.2 Methods for nanoscaffolding

1.3.2.1 Solution impregnation

Solution impregnation involves infiltrating a porous scaffold with a hydride solution. Upon removal of the solvent, the hydride is dispersed over the whole scaffolding material. This method has the downside, that complex hydrides, such as $NaAlH_4$ and $LiBH_4$, have a strong interaction with their solvent tetrahydrofuran (THF), and it may not be possible to remove all of the solvent [23]. This is unavoidable, as the choice of solvents is very limited [31]. Furthermore, a synthesis step and more potential contaminants are added to the process [23].

By solution impregnation into ordered mesoporous silica, it has been demonstrated that nanoconfined $NaAlH_4$ has lower temperatures and faster kinetics for dehydrogenation compared to bulk. Furthermore, hydrogenation was achieved without the presence of a catalyst and under relatively mild conditions: 125-150 °C and 35-55 bar [32]. Baldé et al. solution impregnated $NaAlH_4$ into carbon nanofibers (CNFs) and found a direct relation between particle size of $NaAlH_4$ and the activation energy for H_2 evolution. The activation energy for H_2 release from the synthesized composites was lower than ball-milled and Ti-catalyzed $NaAlH_4$. Particles between 2-10 nm began decomposing already below 70 °C, making it applicable for use in PEM fuel cells. Moreover, the nano-$NaAlH_4$ started hydrogenating already at 20 bar H_2 pressure. However, the applied $NaAlH_4$ loading was very low (8 mass%), and the loading capacity was low as well. This was most likely due to poor nanoconfinement in the

CNFs. In addition, it was presented that particles ≤ 30 nm behave as nanoparticles. This contrasts with the confirmed notion that particles 1-10 μm in size behave already as bulk material [33]. Even lower activation energies than presented in Ref. [33] have been achieved by solution impregnating $NaAlH_4$ into microporous carbon [34], achieving hydrogen release already at ambient temperature [35].

Bhakta et al. utilized a MOF to confine $NaAlH_4$ into nanoparticles and analyze their thermodynamic and kinetic properties. They concluded that both particle size and interactions between the scaffolding and alanate have an effect, but the particle size is more influential. The latter allows fine-tuning the thermodynamic and kinetic properties [36]. Similar dramatic alterations of reaction pathway and kinetics have been shown for $LiBH_4$, which was nanoconfined into highly ordered nanoporous carbon via melt infiltration [37], the method discussed in the following chapter.

1.3.2.2 Melt infiltration

In melt infiltration, the hydride is melted and inserted into the scaffolding's pores via capillary effects. The nanomaterial is then obtained through simple cooling and solidification [23].

It has been demonstrated that melt-infiltration synthesis is an effective and straightforward method for $NaAlH_4$/C composites. The majority of the pore volume of the nanoporous carbon was filled within a few minutes, resulting in a differently structured $NaAlH_4$ upon solidification. This $NaAlH_4$ did not show any crystallinity and was determined to be in intimate contact with the carbon. The carbon's structure remained unchanged. The optimal loading for that system was determined to be 20 mass%, half of the theoretical maximum for the total pore volume of the carbon. The nanosized $NaAlH_4$ started H_2 release already at 110 °C and could be hydrogenated already at 24 bar and 150 °C, achieving 2.4 mass% of H_2 per gram of $NaAlH_4$ within 3 h. It was also noted that some of the hydride had already decomposed during the synthesis [38].

When preparing Mg nanoparticles in carbon matrices through melt-infiltration for the purpose of hydrogen storage, it was discovered that the optimal pore filling took place at ≤ 10 nm, with the smallest pores remaining unfilled. This points towards an optimum pore size, where the lower bound is determined by pore accessibility and the upper bound by the driving capillary suction force [39]. This was further demonstrated with $NaAlH_4$ by Gao et al. when $NaAlH_4$ was confined to pores 2-15 nm in size. It demonstrated entirely different thermodynamic properties, as it decomposed to NaH in a single step skipping the Na_3AlH_6

phase (reaction II) altogether [40]. This is also repeated during hydrogenation. A theoretical model was developed later by Mueller and Ceder. They explained that with alanate particles < 52 nm, there is a new thermodynamic pathway that skips the second decomposition step for $NaAlH_4$ due to the size effect [41], which also corroborates Baldé et al. results achieved through solution impregnation [33] as presented in chapter 1.3.2.1.

In addition to the different decomposition reaction, Gao et al. also demonstrated a change in the hydrogen evolution profile. The H_2 release was at lower temperatures (100-120 °C), and there was no sharp NaH decomposition peak. The latter pointed towards a very high dispersion of the NaH particles, resulting in decomposition without a well-defined peak. Furthermore, the $NaAlH_4$ was demonstrated to have gained stability at the expense of the disappeared Na_3AlH_6 phase, and finally, rehydrogenation was achieved at 24 bar H_2 at 150 °C [40].

T.K. Nielsen has proposed that the interactions between the carbon scaffold and alanate are significantly more influential than the effects of nanoconfinement or pore size reduction [42], but this is not supported by other authors [32,33,40,43], and also his methodology is questionable. This especially regarding calculations, where, for example, the $NaAlH_4$ density presented, 0.905 g cm^{-3}, is incorrect, the correct being 1.24 g cm^{-3} [31].

Also, a $NaAlH_4$/Vulcan XC72R system has been shown to achieve dehydrogenation already at ambient conditions, although most of the hydrogen evolved ~180 °C. However, relatively low efficiencies were achieved, leading to the conclusion that most of the alanate decomposed during the synthesis or at ambient conditions, where it was stored [44].

1.3.2.3 Ball milling

Ball milling is the most widely used method for nanostructuring. In addition to lowering the particle size, the high-energy process creates highly reactive surfaces. The higher density of grain boundaries created can facilitate hydrogen diffusion and improve overall kinetics. However, although nanoparticles may be achieved at first, the material can undergo recrystallization and particle growth over time or during dehydrogenation/hydrogenation cycling, returning to bulk-like behavior [29].

Ball milling is most often used to enhance hydrogen storage properties by reducing particle size [45], doping [45–49], or creating mixed hydride systems [18,45,50,51] that have alternative dehydrogenation pathways. In all cases, thermodynamics and kinetics of dehydrogenation have successfully been improved. Catalysts have also affected the hydrogenation processes, providing similar results to the methods described in the previous two

chapters, although nanoconfinement has no role in these systems. Ball milling also assists in the regeneration process of the original storage material [16]. Most importantly, Pinkerton has described composites, where $NaAlH_4$ has been ball milled together with carbon aerogel. Incorporating porous carbons improved dehydrogenation and cycling properties. Significantly affected was reaction II, where the kinetics of the $Na_3AlH_6 \leftrightarrow NaH$ transition was considerably enhanced. The results were an improvement over both catalyzed and melt-infused systems [52].

Furthermore, high loadings of the active phase could be used since very small amounts of carbon still affected the material's properties in a very modestly reduced manner. Therefore, all of the changes cannot be attributed to nanoconfinement, but the carbon itself has some kind of catalytic effect. This means ball milling provides a flexible and straightforward technique to prepare improved hydride-based H_2 storage systems with high loadings and may easily incorporate dopants. Regarding reversibility, hydrogenation was achieved already at 19.8 bar H_2 and 140. Still, it must be noted that only reaction II was reversible, hence only Na_3AlH_6 formed, and the cycling behavior could be attributed to the $Na_3AlH_6 \leftrightarrow NaH$ transition [52].

1.4 Methods

1.4.1 Ball milling

Ball milling has been widely used as a tool for tuning the hydrogenation properties of materials and the synthesis of new hydrogen storage materials. During the milling process, powder caught between balls or ball and the container wall experience significant tension, compression, and shear forces [3,53]. During high-energy milling, powder particles are repeatedly flattened, cold-welded, fractured, and rewelded. At first, the materials experience elastic deformations. As the load increases, the force of the impacts starts to plastically deform the powder particles leading to work hardening and fracture. A significant amount of the energy is transferred to the powder, and new surfaces are created, and existing particles are refined. New particles generated by this mechanism may continue to reduce in size in the absence of strong agglomerating forces [53,54]. In addition to pulverization and decreased particle size resulting in higher surface-to-volume ratios, the mechanical milling creates mechanical defects, destroys any passivating surface groups through creating new surfaces, and intensely mixes, fractures, and welds the powders ensuring chemical homogeneity [3,53,54]. At the point of equilibrium between fracturing and welding processes, the particle size distribution is narrow, as larger particles have been reduced and smaller particles have agglomerated [54]. Even short processing may result in nanostructuring, increasing chemical reactivity, and changing thermodynamic and kinetic properties. The nanostructuring entails the reduction of both

particle and grain size. However, nanostructured materials do not necessarily consist of nanometric particles. It is understood more as maximized density of grain boundaries, meaning micrometric particles may be divided into many nanograins [3].

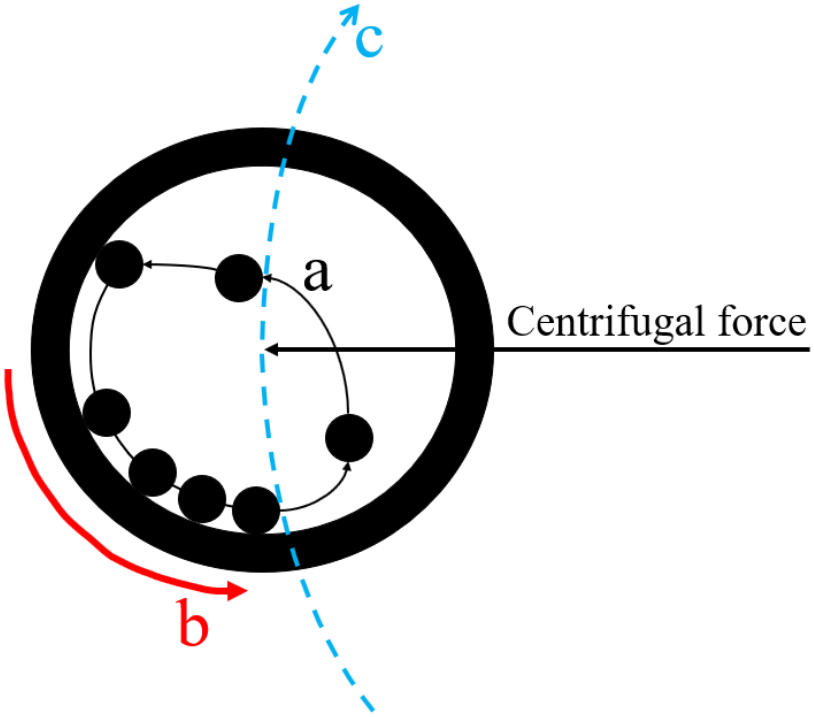

Figure 2. Working principle of a planetary ball mill: a) movement of balls, b) rotation of grinding bowl, c) rotation of support disc.

In a ball milling synthesis, powders are mixed into the mill along with the grinding medium, usually metal or ceramic grinding balls. This mixture is milled for a length of time until the desirable state and composition have been reached. In a planetary ball mill, the grinding bowl is fixated on a rotary disk, and a drive mechanism rotates it around its axis (Figure 2). The centrifugal force produced by the grinding bowl around their own axis and that produced by the support disk both act on the bowl's contents. As the bowl and support disk rotate in opposite directions, the grinding balls run down the inside walls and grind the materials through friction. After that, the balls lift off, travel freely, and collide against the opposing wall, grinding the materials through impact. The grinding medium used can be of several different materials, e.g., agate, steel, tungsten carbide, zirconia, etc. [54]. Parameters affecting milling are the materials milled, the milling materials, and the process variables, such as milling time, speed, etc. These variables are not all independent of each other, and in general, the milling parameters have to be optimized for each system and purpose [54,55]. However, universal procedures for optimization have been explored [56,57]. The most critical parameters to consider in this work

are the milling speed (in rotations per minute, RPM), duration, temperature, grinding bowl and medium, and ball-to-powder ratio.

Speed, duration, and temperature depend on each other and must be balanced out for the desired effect. Higher speeds offer higher energy outputs and shorter milling times. However, higher speed causes a rise in temperature, which may cause unwanted effects to the milled material, and may require adding cooling breaks to the milling [54,55]. Furthermore, although the macroscopical temperatures achieved during milling are not very high, with typical maximums in the range of 100 °C, the local temperature at the point of impact may vary due to the high energies involved. The latter must be estimated with models. Milling time should be chosen to be exactly as long to achieve the desired effect. Dependent on the other parameters, it should be the point when fracturing and cold welding have reached an equilibrium. In addition to directly affecting chemical reactions and phase transitions, higher temperatures also speed up agglomeration. The ball-to-powder ratio mainly affects milling time, with longer times necessary at lower ratios [54].

When choosing the grinding bowl and medium, the hardness, density, and size must be considered. The medium must be harder than the material being milled and preferably of the same material as the grinding bowl to avoid cross-contamination. The density and size of the grinding balls determine the force of impact the balls have during milling. Larger and heavier balls have higher energy, but these also affect the processes taking place during milling. Furthermore, it is recommended to have the ball sizes correlating with the feed size, i.e., larger balls with larger feed sizes and smaller balls with smaller feed sizes [54,55]. Softer milling conditions (smaller balls, lower energies, lower ball-to-powder ratios) have been shown to achieve more amorphous and metastable phases. In contrast, higher energies may favor the creation of more stable crystalline phases, resulting in the decomposition of more sensitive and unstable compounds [54].

The most noteworthy of the parameters not considered as critical in the context of this work, due to the lack of suitable candidates, is the addition of process controlling agents (PCAs). These PCAs may be both solid compounds and solvents. The addition of the latter is called “wet-milling.” However, although it has been shown to increase the effectiveness of milling and decrease agglomeration, it increases contamination of the mix, may add additional purification steps to the synthesis process, and a suitable PCA does not exist for all syntheses [54].

1.4.2 Characterization

1.4.2.1 Temperature-programmed dehydrogenation (TPD)

The temperature-programmed dehydrogenation (TPD) experiment enables us to obtain kinetic and quantitative data about the hydrogen evolution process [34,35]. The temperature is linearly raised during the experiment while a steady stream of inert carrier gas flows through the powder sample [58]. When the activation energy is exceeded, the hydride decomposes, releasing hydrogen into the flowing gas, which then carries it into the detector [34,58]. The AutoChem 2950 HP chemisorption analyzer (Supplementary Section 1) utilizes a thermal conductivity detector (TCD) to measure gas concentrations. The gas flowing through the TCD removes heat from a filament maintained at a constant temperature via an electrical current. The amount of heat removed is determined by the gas's thermal conductivity. The change in the composition of the gas changes its thermal conductivity creating a shift in the power required to maintain the filament at a constant temperature. It is preferred for the carrier gas to have a significantly different thermal conductivity coefficient than the measured gas to have a detectable signal [58]. If the gas analyzed is hydrogen (H_2, 187 $mW \cdot m^{-1} \cdot K^{-1}$ at 300 K), nitrogen (N_2, 26 $mW \cdot m^{-1} \cdot K^{-1}$ at 300 K) is used as the carrier gas [59].

The measured signal is proportional to the concentration of the detected gas. For calculations, a calibration constant is used to convert the thermal conductivity data into values that directly represent the concentration of evolved H_2. To obtain this constant, calibration measurements, where fixed and known amounts of H_2 are injected into the N_2 stream, are performed [58]. From the measured data, both the rate and quantity of evolved H_2 can be calculated, giving a thorough overview of the material's H_2 storage properties [34,35].

1.4.2.2 Gas sorption

Gas adsorption is an extensively used method for the characterization of porous solids and fine powders. Adsorption is the enrichment of molecules, atoms, or ions in the vicinity of an interface. The adsorbed substance is known as the adsorbate, and the adsorbing material is known as the adsorbent. Desorption is the reverse process of adsorption [21]. Physical adsorption (physisorption) is caused by weak van der Waals interactions between the adsorbate and adsorbent, and the adsorbate retains its chemical identity. In chemical adsorption (chemisorption), the adsorbate forms chemical bonds with the surface. The enthalpies of physisorption are typically in the 20 kJ mol^{-1} range, and chemisorption enthalpies are generally in the range of 200 kJ mol^{-1} [60]. Physisorption of gases is used as a characterization method to determine the specific surface area, pore volume, and pore size distribution of materials [21].

N_2 is the most used adsorbate, owing to the wide availability of liquid nitrogen and suitable characteristics (inert, known relatively small molecular cross-sectional area) [61]. In a typical manometric N_2 adsorption experiment, the amount of gas removed from the gas phase is measured at 77 K. N_2 physisorption is a very suitable method for characterizing micro-mesoporous solids (pore widths between 0.7-30 nm). The relation between the amount of gas adsorbed and the equilibrium pressure of the gas at constant temperature is known as the adsorption isotherm. The isotherm is usually plotted as an x-y plot, where the y-axis is the adsorbed amount n_a and the x-axis the relative pressure p/p_0, where p is the equilibrium pressure and p_0 is the saturation vapor pressure at the adsorption temperature ($p_{0,N2}$ is 1 bar at 77 K). This applies at pressures < 1 bar, as to be exact, the quantity determined by a gas sorption measurement is the surface excess amount n_σ. The surface excess amount assumes that adsorption occurs on an imaginary 2D surface (the Gibbs dividing surface), i.e., has no volume (which it does in reality). The approximation that $n_\sigma = n_a$ is appropriate when operating with adsorption of vapors below 1 bar, although an accurate determination of the void volume is required [21].

The Brunauer-Emmett-Teller (BET) method [62] is widely used to calculate the specific surface area of porous materials, being both simple and comparable with previous works. The BET theory assumes that the surface is energetically homogenous, and there is no interaction among adsorbed molecules [63]. The isotherm equation takes into account multilayer adsorption [21,60,61]:

$$\frac{V}{V_{\text{mono}}} = \frac{cz}{(1-z)[1-(1-c)z]}\,, \tag{1}$$

where $z = p/p_0$, V_{mono} is the volume corresponding to monolayer coverage, and c is a constant. The BET equation can be linearized into

$$\frac{z}{(1-z)V} = \frac{1}{cV_{\text{mono}}} + \frac{(c-1)z}{cV_{\text{mono}}} \tag{2}$$

$\frac{z}{V(1-z)}$ is plotted against z. $\frac{(c-1)}{cV_{\text{mono}}}$ can be obtained from the slope, s, and cV_{mono} can be found from the intercept, i. These can be combined to calculate V_{mono}:

$$V_{\text{mono}} = \frac{1}{s+i}$$

The total surface area, S, can be calculated:

$$S = \frac{V_{\text{mono}} N_A \sigma_m}{V_m}, \tag{3}$$

where N_A is the Avogadro number, σ_m is the molecular cross-section of the adsorbate, and V_m is the molar volume of the adsorbate. The specific surface area S_{BET} can be calculated by dividing S with the sample mass. Due to the required linearity, the BET isotherm is applicable at pressure ranges $0.05 \leq p/p_0 \leq 0.03$.

The total pore volume (V_{tot}) can be calculated from the adsorbed amount near the saturation pressure $p/p_0 \approx 0.95$, where the density of the adsorbate is assumed to be equal to its liquid density [64].

1.4.2.3 Powder X-ray Diffraction (PXRD)

X-ray diffraction (XRD) is a widely used method to study the structure of crystalline materials, although noncrystalline, i.e., amorphous materials, may be studied as well [65]. Crystalline materials have an ordered long-range atomic arrangement. A crystal is a periodic crystalline substance in three dimensions and bounded by plane faces [66]. In an X-ray diffraction experiment, the sample is irradiated with monochromatic and collimated X-rays generated in an X-ray tube. Since the wavelength of X-rays is in the same order of magnitude as the distance between atoms in a crystal structure (in the order of Ångstroms, 1 Å = 0.1 nm), then the X-rays diffract when interacting with the electron shell of an atom. Constructive interference between the diffracted X-rays results in diffraction peaks [65].

The diffraction peaks from an XRD experiment are analyzed using the Bragg equation [67]. To reach this equation, let us first consider a simple X-ray experiment (Figure 3).

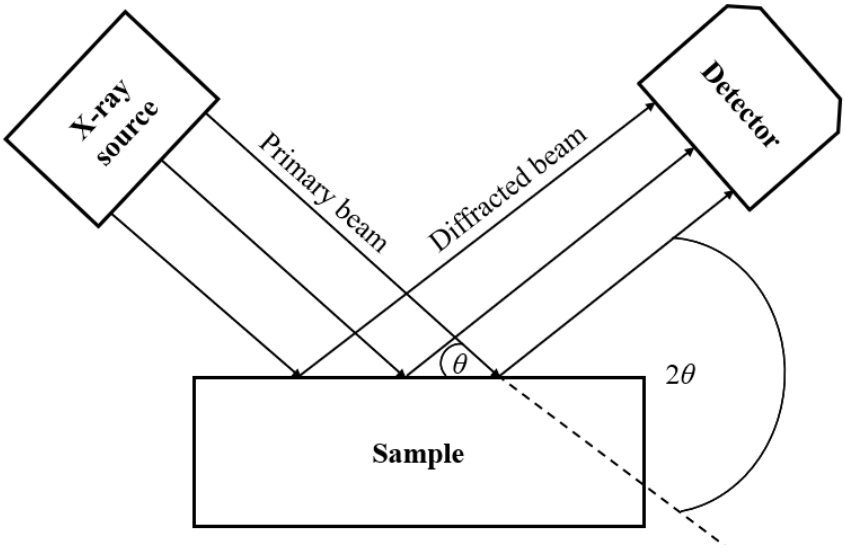

Figure 3. Representative schematic of a simple XRD experiment.

Note the angle 2θ. This is the angle between the primary and diffracted X-ray beam (also called the scattering angle). This angle is utilized when analyzing data, e.g., creating and analyzing

diffractograms, because it is a parameter independent of the experiment's geometrical setup. A diffractogram is a graph where the x-axis is usually 2θ, and the y-axis is intensity. When viewing the same experiment at an atomic level (Figure 4), we notice a path difference between X-ray beams interacting with different parallel lattice planes.

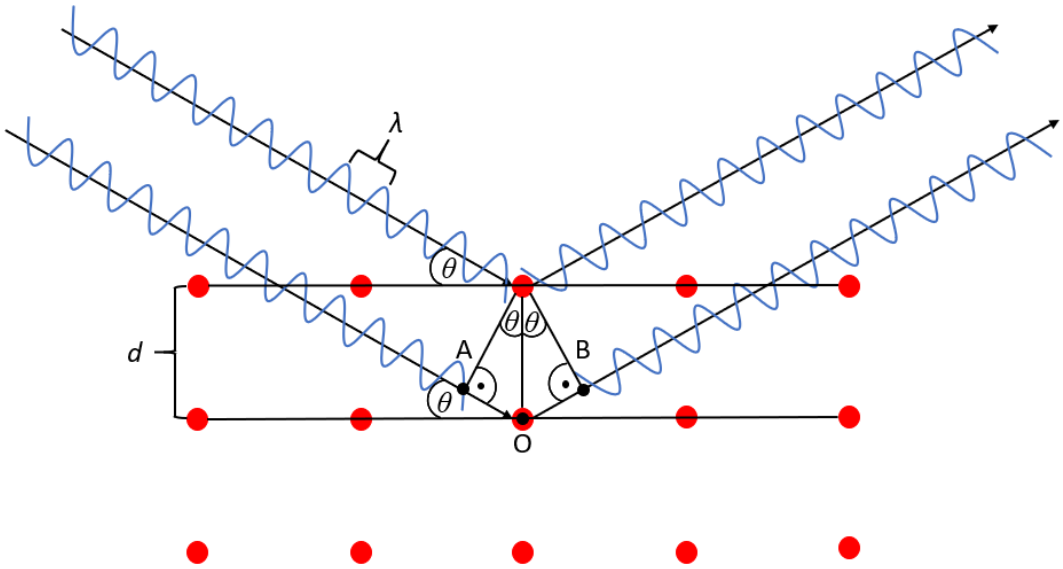

Figure 4. Diffraction from a crystal lattice.

The path difference is:

$$AO + OB = 2AO$$

$$AO = d\sin(\theta) \Rightarrow 2AO = 2d\sin(\theta).$$

Considering the superposition principle, we may state that the waves will interfere constructively when in phase and destructively when not. From this, we derive that for constructive interference, the distance $2d\sin(\theta)$ must be equal to the wavelength multiplied by a positive integer, which gives us the Bragg equation:

$$n\lambda = 2d\sin(\theta), \quad (4)$$

where n is a positive integer, λ is the X-ray wavelength, d is the distance between lattice planes, and θ is the angle between the sample plane and the primary X-ray beam. Thus, the Bragg equation represents the condition at which constructive interference occurs upon diffraction from a crystal lattice and results in a sharp diffraction peak. As in an X-ray experiment, the λ and θ are known quantities, one can calculate the distance of crystal planes d from the peak position on a diffractogram. Using this data and XRD analysis software, which includes databases of diffractograms of known chemical compounds, the sample's phase composition may be determined [65,67]. In a powder X-ray diffraction (PXRD) experiment, the sample is in powder form, meaning the sample consists of randomly oriented crystallites [68].

The XRD experiment requires diffraction from an infinite amount of planes (perfect crystal) for a sharp diffraction peak. However, the distance between atoms is less than 1 nm. Therefore a particle the size of roughly 0.5 μm or more already represents a near-infinite amount of lattice planes. Deviations from this perfectly ordered and infinite 3D structure are visible in the diffractograms. The most significant causes in the context of this work are polycrystallinity and nanoparticles, which are intimately related. As the size of the ordered structure reduces, the diffraction peaks begin to widen, ultimately leading to the point where it cannot be differentiated from the background [65].

1.4.2.4 Dehydrogenation/hydrogenation cycling with iSorb HP1 (Quantachrome, USA)

In order to obtain kinetic and quantitative data and evaluate the durability of a hydrogen storage material over several dehydrogenation/hydrogenation cycles, high pressures and temperatures are required. The iSorb HP1 (Quantachrome, USA) is a volumetric high-pressure gas sorption system capable of performing formation-decomposition studies of hydrides. The system has a manifold of known volume and stable temperature. By using highly sensitive pressure sensors, it is possible to know the exact amount of gas enclosed in any part of the system at any given time. The pressure, temperature, and volume are known variables, and the volume of the sample cell can be calculated via calibration with helium. Hence, during an experiment, the system calculates the theoretical pressure that should be achieved with known gas quantities and compares that to the actual pressure. The difference between pressures represents the amount of hydrogen stored or extracted [69].

2 EXPERIMENTAL SECTION

2.1 Synthesis

Composites with 50, 60, 70, 80, and 90 mass% of $NaAlH_4$ were synthesized using a PULVERISETTE 6 classic line planetary mono mill (Fritsch, Germany). All materials containing $NaAlH_4$ were handled in an MBraun LABmaster sp glovebox (MBraun, Germany), filled with argon (Ar, 5.0, Linde, UK). The $NaAlH_4$ (90%, Sigma-Aldrich, Germany) had been purified with the recrystallization method. Bulk $NaAlH_4$ was dissolved in tetrahydrofuran, THF (anhydrous, ≥ 99.9%, Sigma-Aldrich, Germany), resulting in a 0.05 $g_{NaAlH4}\ mL_{THF}^{-1}$ solution. The solution was filtrated through a glass microfiber filter (GF/B, Whatman) to remove any impurities. The THF was removed via the Buchi R-215 Rotavapor System, which includes the B-491 Heating Bath, V-710 vacuum pump, and V-855 vacuum controller (Buchi, Switzerland). The $NaAlH_4$ solution in THF was held at 260 mbar and 50 °C until most of the THF was removed. Then the sample was held at room temperature and full vacuum for 15 h.

An appropriate ratio of the carbon black Vulcan XC72R (Cabot, USA) and the recrystallized $NaAlH_4$ was weighed and placed into a ZrO_2 grinding bowl containing 25 10 mm ZrO_2 grinding balls. The system was hermetically sealed via a clamp, and the materials were ground in the planetary mill for 40 min, allowing for 10 min cooling breaks every 5 minutes.

2.2 Temperature-programmed dehydrogenation

The temperature-programmed dehydrogenation experiments were performed with the AutoChem 2950 HP chemisorption analyzer (Micromeritics, USA), which utilizes a thermal conductivity detector. 10-30 mg of a given sample was measured in a nitrogen (N_2, 6.0, Linde, UK) gas flow of 50 mL min^{-1}. A baseline was established by maintaining the temperature at 0 °C for 2 h. Then, a temperature ramp rate of 2 °C/min was applied, and the desorbed H_2 was measured from 0 to 600 °C. Further analysis and calculations were done utilizing the software OriginPro 2015 (OriginLab Corporation, USA).

For calculations, a calibration constant was necessary (described in chapter 1.5.2.4). The calibration constant was acquired by injecting fixed, known amounts (from 0.1 mL to 10 mL) of H_2 (6.0, Linde, UK) into an N_2 stream of 50 mL min^{-1}. Then, the amount of injected H_2 was plotted against the TCD signal change, and the calibration constant was calculated.

2.3 Gas sorption

All used materials were characterized using the N_2 sorption method utilizing the ASAP 2020 (Micromeritics, USA) surface area and porosity analyzer. The BET theory [62] was used to calculate the specific surface area (S_{BET}). The total pore volume (V_{tot}) was calculated from the adsorbed amount at $p/p_0 = 0.95$, which estimates the volume of pores ≤ 40 nm in width.

2.4 Powder X-ray diffraction

The Vulcan XC72R, $NaAlH_4$, and $NaAlH_4$/Vulcan XC72R composites were characterized using PXRD. The measurements were performed with a D8 Advance (Bruker, USA) diffractometer using a low-background airtight specimen holder. The samples were prepared in an Ar-filled glovebox. Ni-filtered Cu Kα radiation was used and detected with a LynxEye detector. Measurements were done in the range of 13-80° 2θ with a step of 0.016°. The collected data were analyzed with the software package Diffrac Suite EVA and the PDF4+ 2020 database [70]. The measurements were performed, and some of the data analysis was done by Mr. Jaan Aruväli from the Department of Geology.

2.5 Dehydrogenation/hydrogenation cycling

The dehydrogenation/hydrogenation cycling experiments were performed with the iSorb HP1 (Quantachrome, USA) high-pressure gas sorption system. 300-400 mg of composite material was placed into an autoclave and attached to the machine. All sample preparation and handling were done in a glovebox. Then, dehydrogenation under high temperature and low pressure and hydrogenation under high temperature and high H_2 pressure were performed. The parameters of each cycling experiment are presented in Table 1.

The dehydrogenation procedure began with vacuuming the autoclave. Then the 50 mass% composites were dosed to 0.75 bar H_2, and the temperature was ramped to the designated level at a rate of 10 °C min^{-1}. The 60 mass% sample was measured in a vacuum. If the pressure value varied more than 0.25 bar from the designated amount, the autoclave was evacuated to restore the initial dose amount. When the measurement was finished, the autoclave was evacuated, filled with inert gas, and was cooled down to ambient temperatures. Then the sample was evacuated, dosed with the assigned H_2 pressure, and the temperature raised to the designated temperature (Table 1) at a ramp rate of 10 °C min^{-1}. The sample was held under pressure until a dehydrogenation experiment was begun or the sample cell was depressurized and removed entirely. After the cycling experiments, the cycled composites were characterized by TPD and PXRD as described in 2.2 and 2.4.

Table 1. Parameters for the dehydrogenation (dehydro) and hydrogenation (hydro) cycles. *T* is temperature, *p* is pressure, and *t* is time.

Experiment no.	**$NaAlH_4$ mass%**	**$T_{dehydro}$ (°C)**	**T_{hydro} (°C)**	**$p_{H2,dehydro}$ (bar)**	**$p_{H2,hydro}$ (bar)**	**$t_{dehydro}$ (h)**	**t_{hydro} (h)**	**No. of cycles**
1	50	160	160	0.75	160	10	10	1
2	50	150	150	0.75	60	10/4	10	10
3	60	190	190	0	60	4	10	5

3 RESULTS AND DISCUSSION

3.1 Characterization of synthesized composites

3.1.1 Temperature-programmed dehydrogenation

The temperature-programmed dehydrogenation results from pristine $NaAlH_4$, ball-milled $NaAlH_4$, and composites of 50 mass% and 90 mass% are presented in Figure 5a. It is clear that simply milling the alanate lowers the dehydrogenation temperature significantly, as the release of H_2 starts already from ambient temperatures. However, the release of H_2 at low temperatures is kinetically hindered. More intense dehydrogenation begins from ~135 °C. The evolution peaks are considerably wider over a broader and lower temperature range than pristine $NaAlH_4$. This indicates that the particle size has been successfully reduced via ball milling. However, it is also evident from Figure 5b that a considerable amount of $NaAlH_4$ has also decomposed during milling, resulting in a diminished total H_2 amount compared to bulk $NaAlH_4$ (Table 2). However, if compared to the 90 mass% composite, it is interesting to note that the small amount of carbon has helped limit the decomposition of alanate during ball milling compared to the ball-milled bulk alanate. This indicates that the carbon scaffolding has a stabilizing effect for the freshly milled particles, or it assists in dissipating the impact energy of the grinding balls. Also, synergetic effects similar as described in Ref. [52] may also play a role.

Table 2. Measured H_2 efficiencies compared to the $NaAlH_4$ mass% in a composite. Efficiency is defined as the percentage of H_2 evolved compared to the theoretical maximum.

$NaAlH_4$ mass%	**Measured efficiency**	**H_2 amount in mass% of $NaAlH_4$**
50%	75%	5.5
60%	76%	5.6
70%	76%	5.6
80%	89%	6.6
90%	92%	6.8
100%	97%	7.2
100% ball-milled	72%	5.3

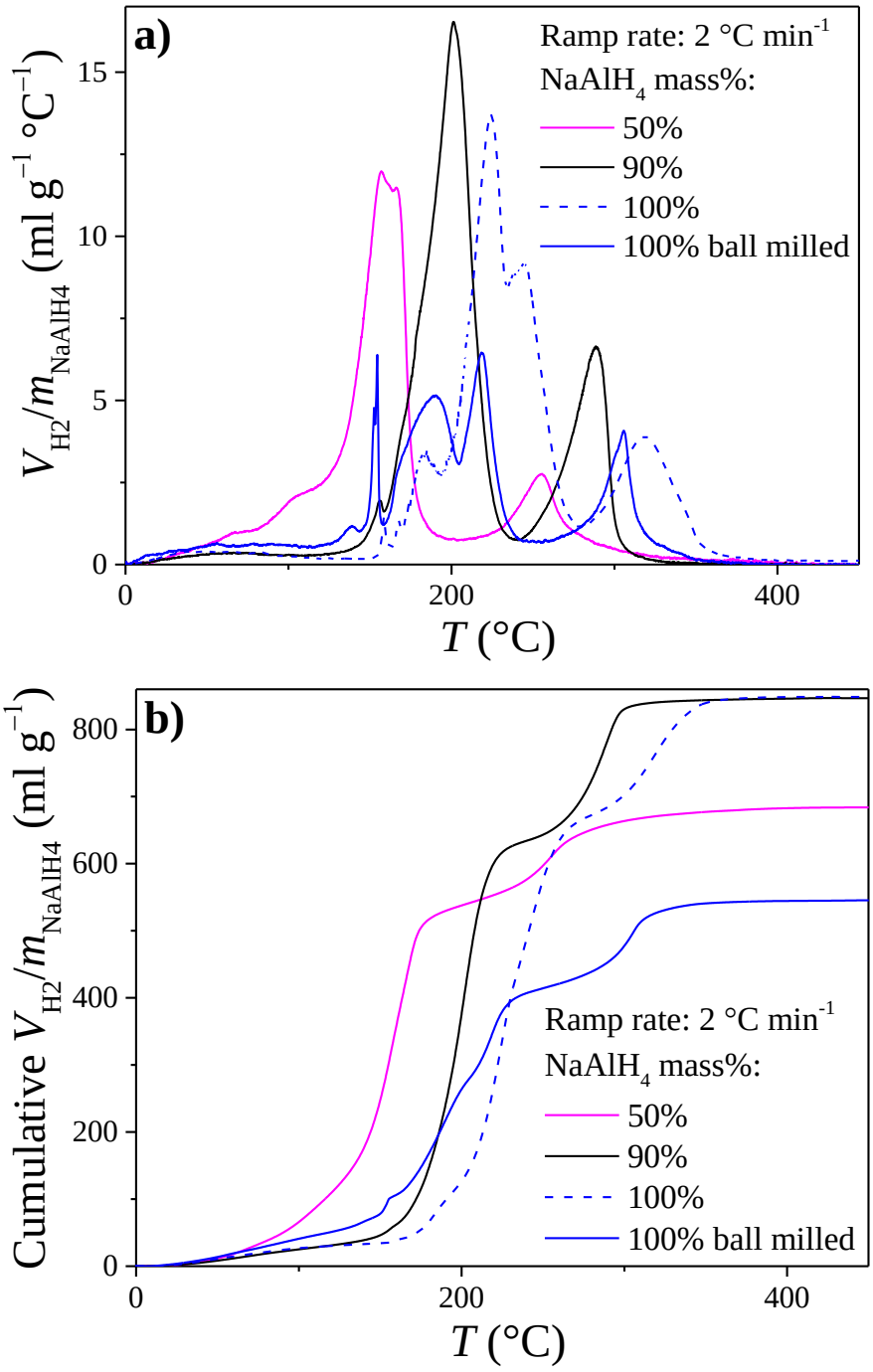

Figure 5. Volume of released hydrogen normalized with the mass of $NaAlH_4$ a) differential and b) cumulative. Pristine $NaAlH_4$, ball-milled $NaAlH_4$, lowest $NaAlH_4$ mass%, and highest $NaAlH_4$ mass% composites are compared. Ball-milled $NaAlH_4$ has some dehydrogenation taking place at temperatures > 500 °C, which is not shown.

When looking at the composite series as a whole (Table 2, Figure 6), there is a clear correlation between alanate mass% and dehydrogenation temperature. It can be concluded that the $NaAlH_4$ particle size has been successfully and significantly reduced. This resulted in dehydrogenation starting from ambient conditions, although the most significant

dehydrogenation occurred between 120-190 °C for the 50 mass% composite and 145-235 °C for the 90 mass% composite. The aim of using ball milling and high loadings was to analyze a realistically simple synthesis method and practically competitive active material loadings. In reality, all of the pore volume of the Vulcan would be filled < 50 mass% of $NaAlH_4$, hence, nanoconfining all of the $NaAlH_4$ into them would be impossible. However, as Vulcan is a carbon black consisting of spherical nanoparticles, some alanate may be deposited as a thin layer on the particles, resulting in nanoscaling, and carbon has been shown to have catalytic effects (see chapter 1.3.2.3, [52]). The exact type and size of the nanoparticles are difficult to determine from existing data.

A distinct trend can be discerned from these results. The scaffolding effects of the porous carbon are more intense at lower $NaAlH_4$ content. This is noticeable not only on the TPD curve (Figure 6a), where it is presented as dehydrogenation at ambient conditions but also in the cumulative graph (Figure 6b), where the effective H_2 amount per unit mass of $NaAlH_4$ is lower for the lower mass%. This indicates that the decomposition conditions have lowered to ambient, and material may be decomposing already at milling and storage conditions, resulting in lower H_2 yield.

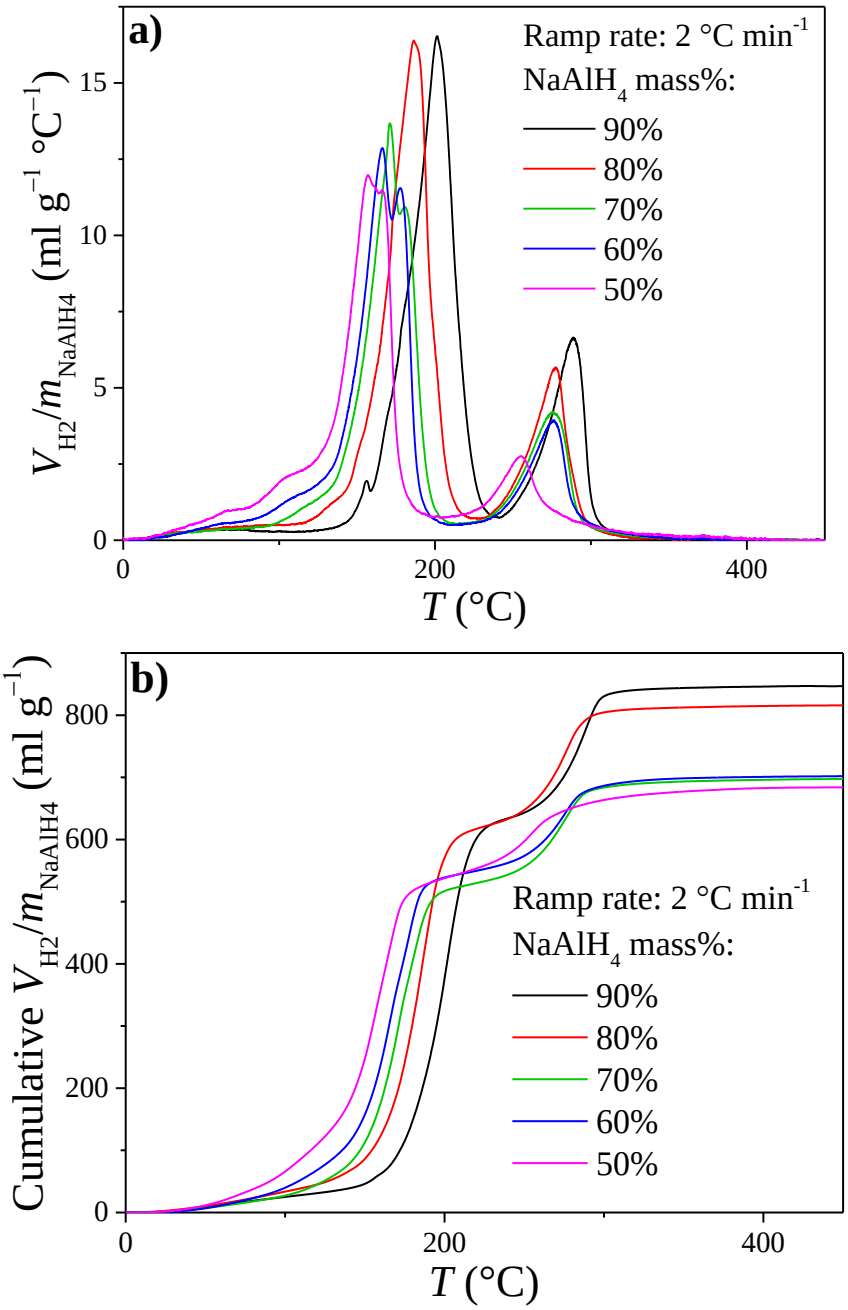

Figure 6. Volume of released hydrogen normalized with the mass of $NaAlH_4$ a) differential and b) cumulative. $NaAlH_4$/Vulcan XC72R composites of different $NaAlH_4$ mass% are compared.

3.1.2 Gas sorption

The gas sorption analysis showed a significant reduction in specific surface area (S_{BET}) and total pore volume (V_{tot}). This indicates that the pores of the carbon material have at least mostly been covered or blocked, resulting in some nanoconfinement. The isotherms for the measured samples are presented in Supplementary Section 2 together with the pore size distribution of the carbon black.

Table 3. Results of the gas sorption measurements for the composites, ball-milled pristine $NaAlH_4$ and Vulcan XC72R.

$NaAlH_4$ mass%	**S_{BET} ($m^2\ g^{-1}$)**	**V_{tot} ($cm^3\ g^{-1}$)**
0 (Vulcan XC72R)	226	0.34
50	10	0.03
60	11	0.04
70	8	0.02
80	15	0.04
90	13	0.04
100	11	0.03

3.1.3 Powder X-ray Diffraction

The XRD results from the composite series (Figure 7) reveal only two crystalline phases: $NaAlH_4$ and Al. Al is discernible at 50, 60, 70, and 80 mass% of $NaAlH_4$, not in the 90 mass% composite and pristine $NaAlH_4$. Furthermore, the intensities of Al diffraction peaks decrease with the increase of $NaAlH_4$ mass%, which indicates lower Al content. Thus, we can presume that at lower mass% of $NaAlH_4$, the nanoconfinement of $NaAlH_4$ particles is more successful, and the relative amount of $NaAlH_4$ that decomposes at ambient conditions or during milling is higher. In addition, the lack of the Na_3AlH_6 and NaH intermediate phases supports the theory that the smallest particles are decomposing at ambient conditions, resulting in so small or polycrystalline particles that no sharp Bragg peaks are detected. However, as stated in chapter 3.1.1, the $NaAlH_4$ loadings are so high that all $NaAlH_4$ cannot be nanoconfined into this pore range anyway.

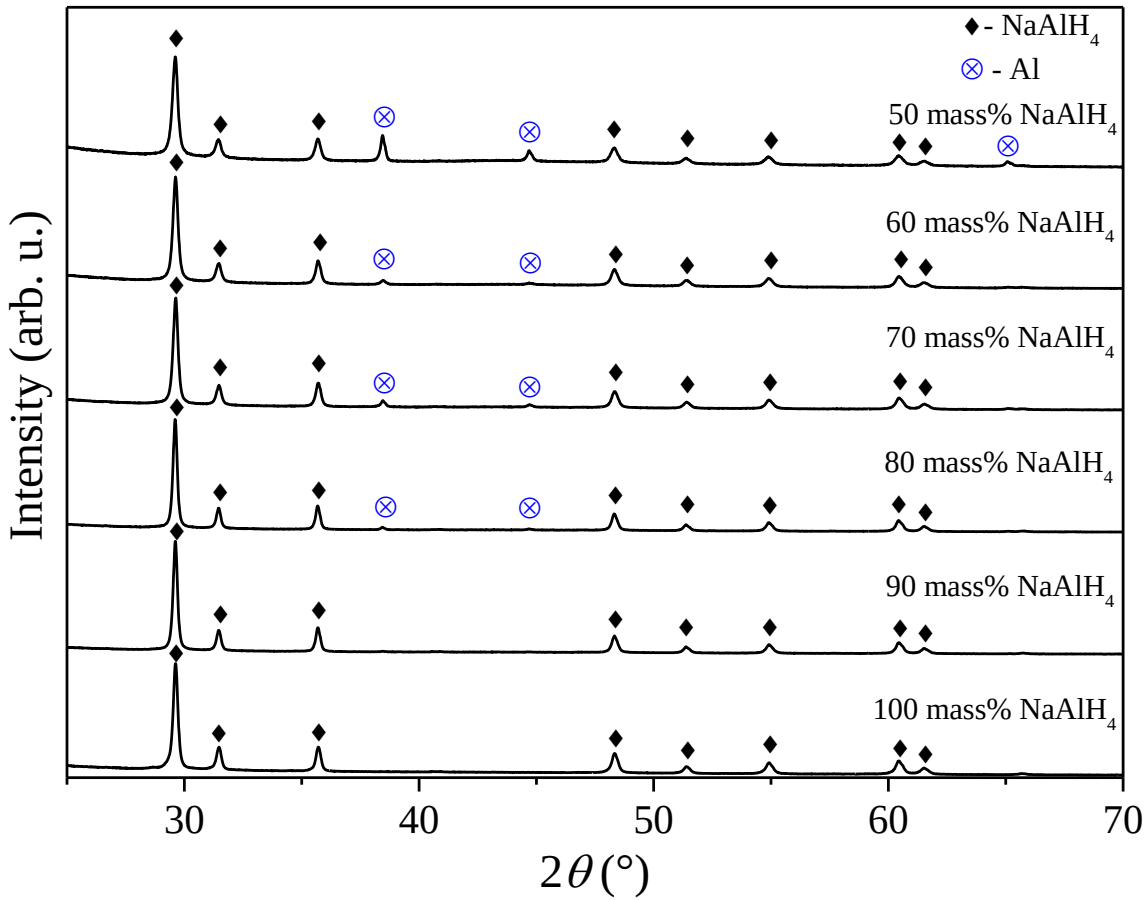

Figure 7. XRD diffractograms of $NaAlH_4$/Vulcan XC72R ball-milled composites and pristine ball-milled $NaAlH_4$.

3.2 Dehydrogenation/hydrogenation cycling

3.2.1 Results of the cycling experiments

The three cycling experiments yielded different information about the composites. The first cycling at 150 °C and 160 bar revealed that the 50 mass% is cyclable. However, the material loses some of its hydrogen storage capacity (Figure 8) without any significant discernible change in its XRD profile (Figure 12). This will be discussed further in the following chapters.

The cycling experiment at 150 °C and 60 bar was an exploratory study to study the possible lower bound for cycling and the stability of the 50 mass% composite over 10 cycles. Although the composite was proven to be successfully reversible under these relatively mild conditions, it was determined that the composite's hydrogen storage capacity degraded over time from 3.4 mass% of $NaAlH_4$ (at the 4-hour mark) to 1.7 mass%. The most severe reduction of H_2 storage capacity was after the 1st cycle. There was no discernible difference caused by the varying dehydrogenation durations, other than the cycles where dehydrogenation was

performed for 10 h, there was additional hydrogen that had evolved past the 4 h mark. This may be due to some remaining kinetic limitations.

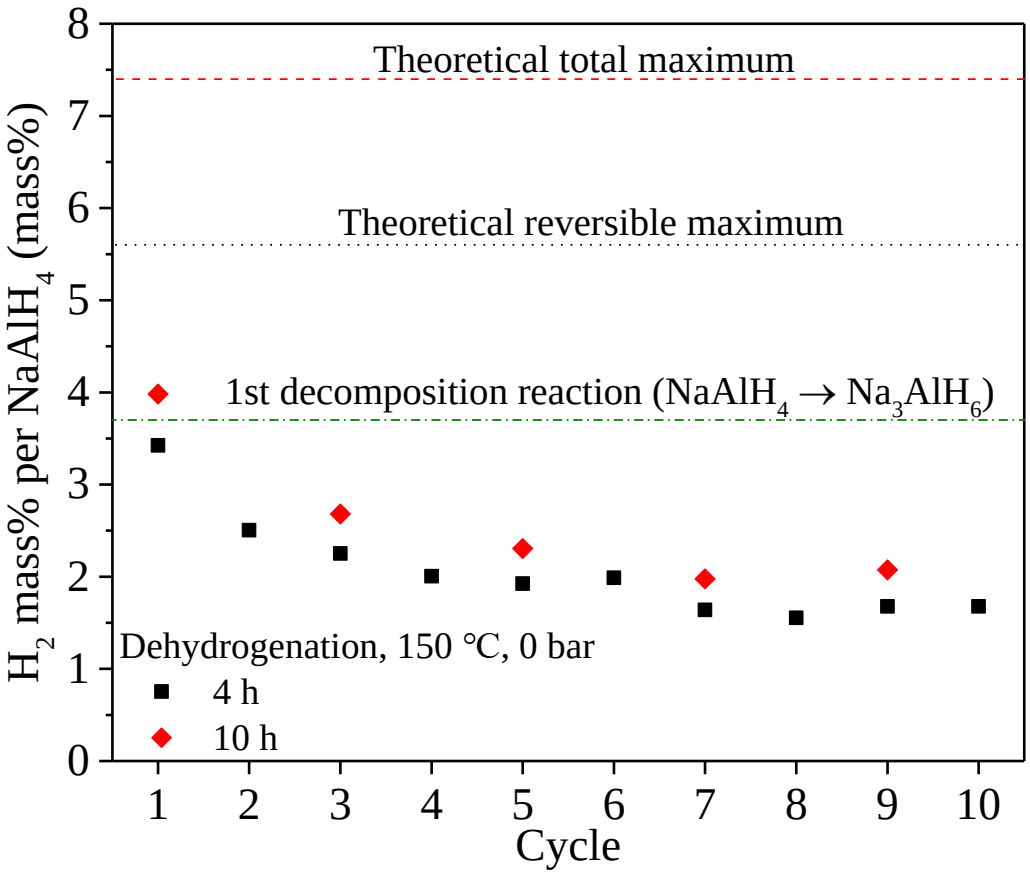

Figure 8. Dehydrogenation results of each cycle for 50 mass% $NaAlH_4$/Vulcan XC72R composite. Hydrogenation was performed at 150 °C, 60 bar for 10 h.

The cycling experiment (Figure 9) at 190 °C and 60 bar were performed to analyze the degradation of the 60 mass% composite and estimate the possible effects of melt infiltration during the first dehydrogenation cycle. When heating past the melting point, the results show that most of the irreversible decomposition of the active material takes place at the very first dehydrogenation. After that, the H_2 storage capacity remained stable for the remaining 4 cycles.

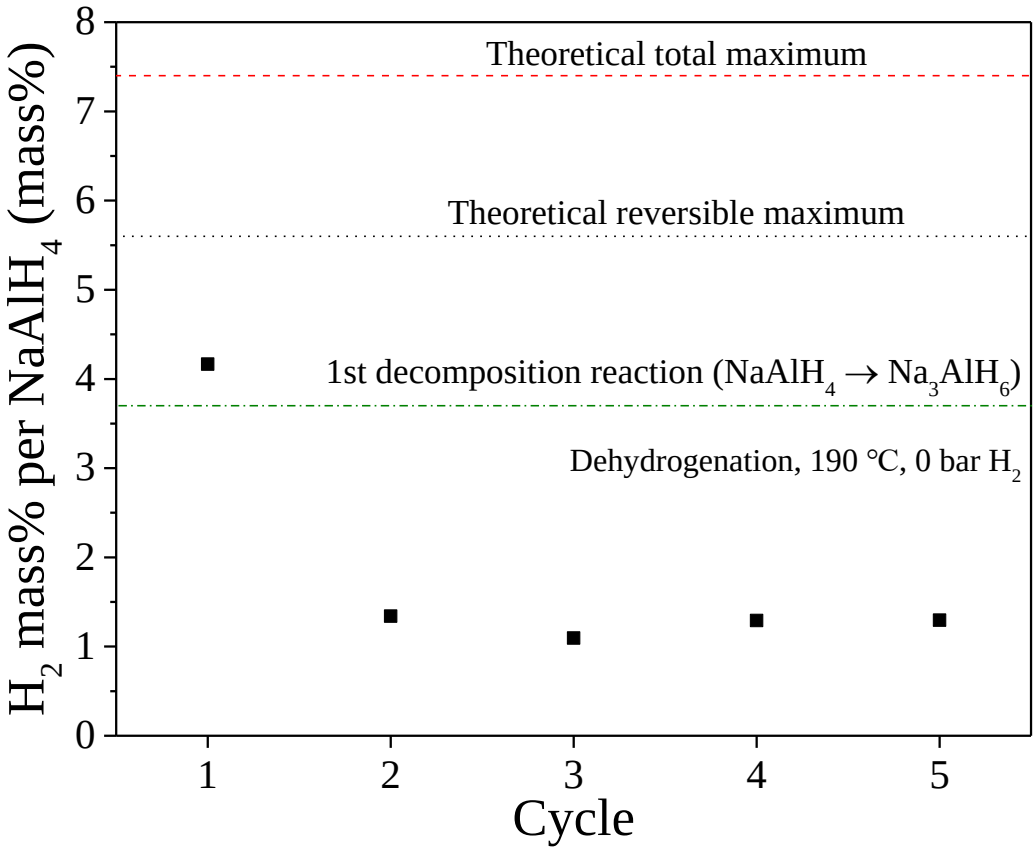

Figure 9. Dehydrogenation results of each cycle for 60 mass% $NaAlH_4$/Vulcan XC72R composite. Hydrogenation was performed at 190 °C, 60 bar for 10 h.

Time dependence of hydrogen evolution is presented in Supplementary Section 3 for both experiments. They demonstrate the gradual diminishing of dehydrogenation speed for the cycling at 150 °C and stable kinetics for the cycling at 190 °C.

3.2.2 Post-cycling temperature-programmed dehydrogenation

The TPD curves of the cycled 50 mass% samples show that the total amount of H_2 reversibly stored in the composite has diminished post-cycling. After 1 cycle, 4.6 mass% of H_2, and after 10 cycles, 4.3 mass% of H_2 was recovered, compared to 5.5 mass% in the pristine composite. As the H_2 evolved during the cycling experiment remained at the range of 1.7 mass%, some of the H_2 did not evolve during the cycling experiment (irreversible reaction III accounts for only 1.8 mass%). This indicates that hydrogenation is kinetically hindered under these testing conditions (Figure 10). As the TPD profile changes, shifting towards higher temperatures, it is reasonable to conclude that particle size has seen some growth. This is most likely due to the decomposition products migrating and merging into larger particles. Although

the scaffolding material has maintained the main dehydrogenation peak at 165 °C even after 10 cycles, the intensity is considerably lower across all temperatures.

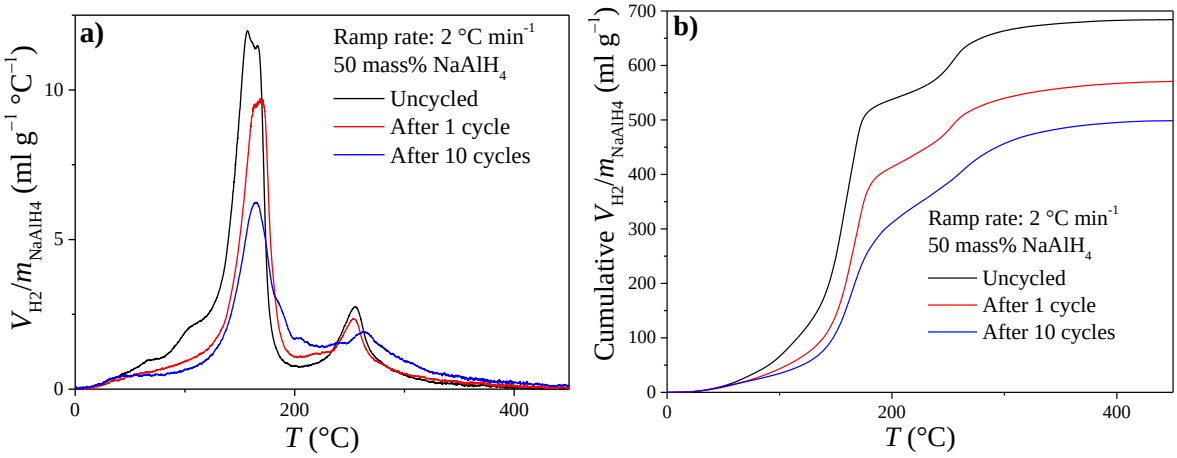

Figure 10. Volume of released hydrogen normalized with the mass of $NaAlH_4$ a) differential and b) cumulative. 50 mass% $NaAlH_4$ composites are presented before cycling, after 1 cycle, and after 10 cycles. See cycling parameters in Table 3

When cycled at 190 °C, the degradation of the 60 mass% composites after cycling is even more apparent. As it was heated over the melting point of $NaAlH_4$, it was passed the kinetic hindrances restricting its decomposition. However, although the total stored H_2 capacity has diminished (from 5.6 mass% to 2.7 mass%), it is still noteworthy that the shape of the curve has not been drastically altered, and H_2 evolves over a wide temperature range. This indicates that the alanate, which has survived degradation, is still nanoscaffolded and retains the same properties as before cycling.

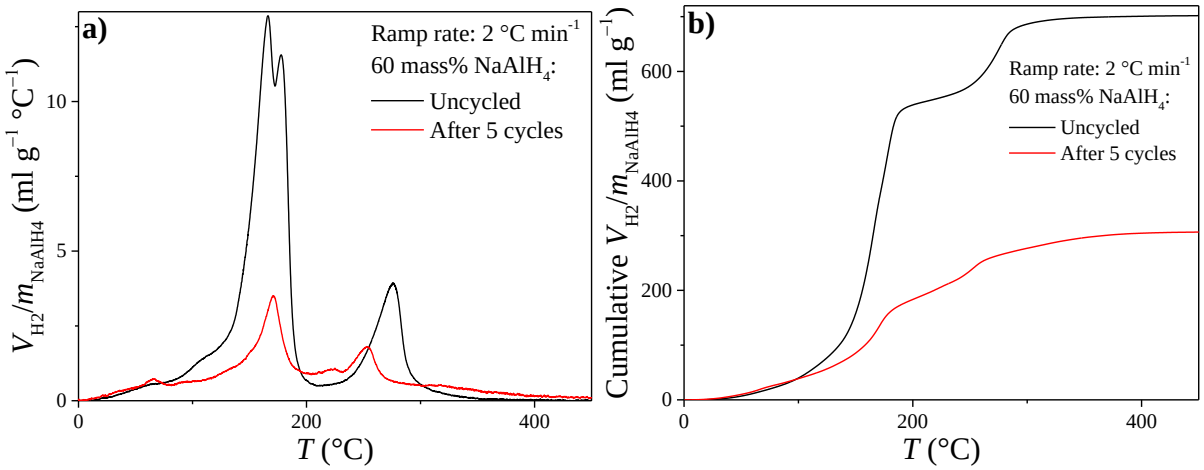

Figure 11. Volume of released hydrogen normalized with the mass of $NaAlH_4$ a) differential and b) cumulative. 60 mass% $NaAlH_4$ composites are presented before cycling and after 5 cycles. See cycling parameters in Table 3.

3.2.3 Post-cycling powder X-ray diffraction

From the cycling experiment at 150 °C (Table 3), it is eminent that in addition to $NaAlH_4$ and Al, the Na_3AlH_6 phase is also present after 10 cycles. Although after one cycle, the intermediate phase Na_3AlH_6 is not present, then after 10 cycles, the particles have grown so large that they give clearly detectable Bragg peaks. This, together with the increase of Al peak intensities, indicates significant material degradation over time. Most likely, the nanoconfinement of $NaAlH_4$ was not restrictive enough or did not result in small enough particle sizes to bypass the reaction II. As the composite was subject to extended intervals of high temperature (up to 150 °C) during cycling, the decomposition products migrated to form larger particles. In the case of successfully nanoconfined particles with sizes ≤ 52 nm, the Na_3AlH_6 phase is skipped and should not be detectable. These larger particles were kinetically too hindered to hydrogenate back into $NaAlH_4$ under these cycling conditions (see Table 3).

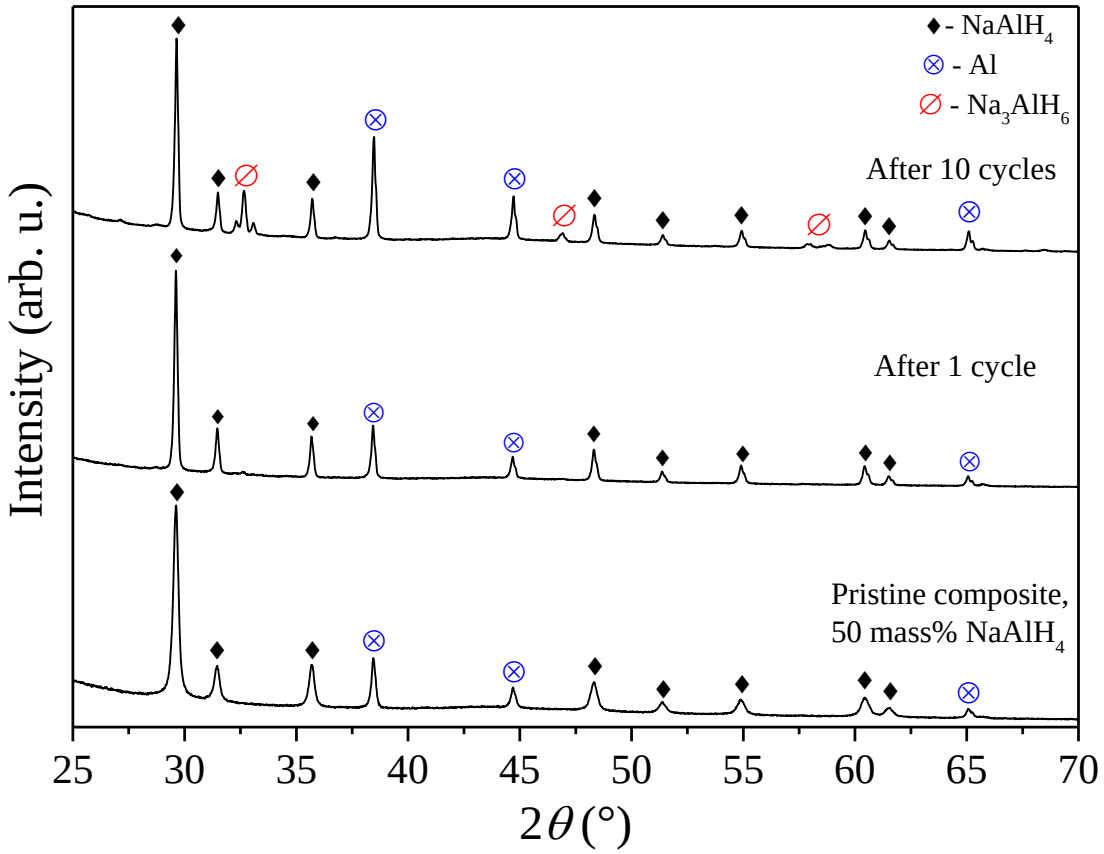

Figure 12. XRD diffractograms of 50 mass% $NaAlH_4$/Vulcan XC72R composite before cycling, after 1 cycle, and after 10 cycles. See cycling parameters in Table 3.

The diffractogram indicates significant degradation from the cycling at 190 °C, as the $NaAlH_4$ peaks are noticeably reduced, while the Na_3AlH_6 and Al peaks are relatively intense. What can be assumed from these results is that it is likely that there has been significant irreversible

decomposition, where Al has segregated into large separate particles. The stable H_2 capacity visible during cycling is from the larger nanoparticles. The cycling takes mainly place in the transition $Na_3AlH_6 \leftrightarrow NaH$, as the formation of $NaAlH_4$ is hindered under these conditions.

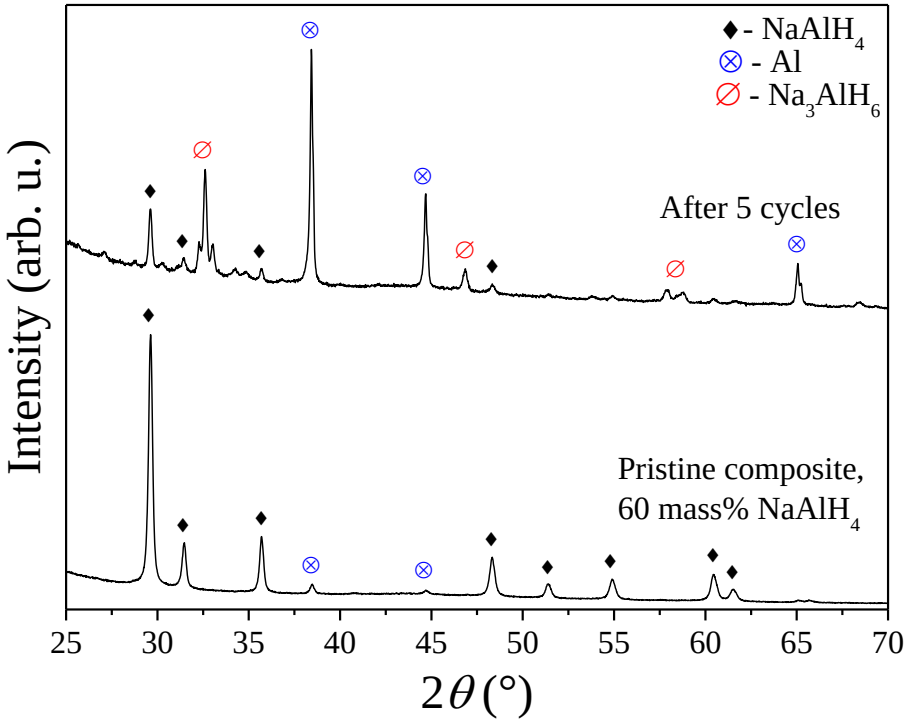

Figure 13. XRD diffractograms of 60 mass% $NaAlH_4$/Vulcan XC72R composite before cycling and after 5 cycles. See cycling parameters in Table 3

3.3 Conclusion

Ball milling synthesis has been shown to create an improved H_2 storage system, with H_2 evolution present even at ambient temperatures. The composites can be cycled under relatively mild conditions (150 °C, 60 bar H_2). Although nanoscaffolding plays a role, the diminishing H_2 storage capacity during cycling and appearance of the Na_3AlH_6 phase indicates that the particles are larger than 50 nm. Some agglomeration of the phases resulting from decomposition occurs, reducing cyclability. Most of the cycling is the transition $Na_3AlH_6 \leftrightarrow NaH$, or reaction II. The resulting improved H_2 storage properties are most likely due to nanoscaling from ball milling, some nanoconfinement, and the catalytic/synergetic effect of the $NaAlH_4$/C interface. The system has high loadings, and in the future, it would be of interest to study if more of the material could be nanoconfined in pores by either changing the synthesis or changing the carbon and add doping with a transition metal. This should enhance both dehydrogenation and hydrogenation properties and hopefully improve the stability of the composite.

SUMMARY

$NaAlH_4$/Vulcan XC72R composites of varying $NaAlH_4$ mass% were synthesized utilizing the ball milling method. These composites were characterized using temperature-programmed dehydrogenation, gas sorption, X-ray diffraction, and dehydrogenation/hydrogenation cycling methods. The aim was to understand the extent of the effect of ball milling and nanoscaffolding on the composite materials' dehydrogenation properties and then to study their stability and reversible H_2 storage capacity over several cycles.

The results showed that the ball milling and nanoscaffolding had successfully altered the H_2 storage properties of $NaAlH_4$, with H_2 evolving already at ambient conditions and dehydrogenation temperatures lowered for all loadings. Even very small mass% of carbon (10%) improved the material properties compared to pure ball-milled alanate. Still, most of the hydrogen evolved at temperatures > 100 ℃. Hence there is still room for improvement to reach the operating temperatures of PEM fuel cells (< 90 ℃). The dehydrogenation/hydrogenation cycling experiments achieved reversible storage at modest conditions: 150 ℃ and 60 bar H_2. However, the composites experienced a loss of H_2 storage capacity during cycling, which is most likely due to segregation of decomposition products, agglomeration of the active phase, and hindered hydrogenation kinetics of larger particles. However, effective results have been achieved with a simple and straightforward synthesis process. Optimizing the choice of carbon, synthesis parameters and adding, for example, catalysts may improve the properties of the composites even further.

REFERENCES

[1] ERR, Vesinikutehnoloogia huvikorjele laekus 23 suurprojekti, Estonian Public Broadcasting. (2021). https://www.err.ee/1608161788/vesinikutehnoloogia-huvikorjele-laekus-23-suurprojekti (accessed June 4, 2021).

[2] A hydrogen strategy for a climate-neutral Europe, (2020). https://ec.europa.eu/energy/sites/ener/files/hydrogen_strategy.pdf.

[3] R.A. Varin, T. Czujko, Z.S. Wronski, Nanomaterials for Solid State Hydrogen Storage, Springer US, Boston, MA, 2009. http://link.springer.com/10.1007/978-0-387-77712-2.

[4] W.L. Kling, E. Pelgrum, B.C. Ummels, Integration of large-scale wind power and use of energy storage in the Netherlands' electricity supply, IET Renewable Power Generation. 2 (2008) 34–46. https://doi.org/10.1049/iet-rpg:20070056.

[5] Target Explanation Document: Onboard Hydrogen Storage for Light-Duty Fuel Cell Vehicles, (2017).

[6] J.O. Abe, A.P.I. Popoola, E. Ajenifuja, O.M. Popoola, Hydrogen energy, economy and storage: Review and recommendation, International Journal of Hydrogen Energy. 44 (2019) 15072–15086. https://doi.org/10.1016/j.ijhydene.2019.04.068.

[7] E. Rivard, M. Trudeau, K. Zaghib, Hydrogen Storage for Mobility: A Review, Materials. 12 (2019) 1973. https://doi.org/10.3390/ma12121973.

[8] L.H. Jepsen, M. Paskevicius, T.R. Jensen, Nanostructured and Complex Hydrides for Hydrogen Storage, in: Nanotechnology for Energy Sustainability, 1st ed., WILEY-VCH Verlag GmbH & Co KGaA, Weinheim, Germany, 2017: pp. 415–432.

[9] B. Sakintuna, F. Lamaridarkrim, M. Hirscher, Metal hydride materials for solid hydrogen storage: A review☆, International Journal of Hydrogen Energy. 32 (2007) 1121–1140. https://doi.org/10.1016/j.ijhydene.2006.11.022.

[10] J. Ren, N.M. Musyoka, H.W. Langmi, M. Mathe, S. Liao, Current research trends and perspectives on materials-based hydrogen storage solutions: A critical review, International Journal of Hydrogen Energy. 42 (2017) 289–311. https://doi.org/10.1016/j.ijhydene.2016.11.195.

[11] J. Bellosta von Colbe, J.-R. Ares, J. Barale, M. Baricco, C. Buckley, G. Capurso, N. Gallandat, D.M. Grant, M.N. Guzik, I. Jacob, E.H. Jensen, T. Jensen, J. Jepsen, T. Klassen, M.V. Lototskyy, K. Manickam, A. Montone, J. Puszkiel, S. Sartori, D.A. Sheppard, A. Stuart, G. Walker, C.J. Webb, H. Yang, V. Yartys, A. Züttel, M. Dornheim, Application of hydrides in hydrogen storage and compression: Achievements, outlook and perspectives, International

Journal of Hydrogen Energy. 44 (2019) 7780–7808. https://doi.org/10.1016/j.ijhydene.2019.01.104.

[12] K. Suárez-Alcántara, J.R. Tena-Garcia, R. Guerrero-Ortiz, Alanates, a Comprehensive Review, Materials. 12 (2019) 2724. https://doi.org/10.3390/ma12172724.

[13] C. Weidenthaler, M. Felderhoff, Complex Hydrides, in: Handbook of Hydrogen Storage, John Wiley & Sons, Ltd, 2010: pp. 117–157. https://doi.org/10.1002/9783527629800.ch5.

[14] B. Bogdanović, M. Schwickardi, Ti-doped alkali metal aluminium hydrides as potential novel reversible hydrogen storage materials1, Journal of Alloys and Compounds. 253–254 (1997) 1–9. https://doi.org/10.1016/S0925-8388(96)03049-6.

[15] B.H. Liu, Z.P. Li, A review: Hydrogen generation from borohydride hydrolysis reaction, Journal of Power Sources. 187 (2009) 527–534. https://doi.org/10.1016/j.jpowsour.2008.11.032.

[16] C. Lang, Y. Jia, J. Liu, H. Wang, L. Ouyang, M. Zhu, X. Yao, $NaBH_4$ regeneration from NaBO2 by high-energy ball milling and its plausible mechanism, International Journal of Hydrogen Energy. 42 (2017) 13127–13135. https://doi.org/10.1016/j.ijhydene.2017.04.014.

[17] T. Ichikawa, Amides, Imides and Mixtures, in: M. Hirscher (Ed.), Handbook of Hydrogen Storage, Wiley-VCH Verlag GmbH & Co. KGaA, Weinheim, Germany, 2010: pp. 159–185. https://doi.org/10.1002/9783527629800.ch6.

[18] Z. Xiong, J. Hu, G. Wu, P. Chen, W. Luo, K. Gross, J. Wang, Thermodynamic and kinetic investigations of the hydrogen storage in the Li–Mg–N–H system, J. Alloys Compd. 398 (2005) 235–239. https://doi.org/10.1016/j.jallcom.2005.02.010.

[19] Y. Li, G. Zhou, F. Fang, X. Yu, Q. Zhang, L. Ouyang, M. Zhu, D. Sun, De-/re-hydrogenation features of NaAlH4 confined exclusively in nanopores, Acta Mater. 59 (2011) 1829–1838. https://doi.org/10.1016/j.actamat.2010.11.049.

[20] L. Zhao, F. Xu, C. Zhang, Z. Wang, H. Ju, X. Gao, X. Zhang, L. Sun, Z. Liu, Enhanced hydrogen storage of alanates: Recent progress and future perspectives, Progress in Natural Science: Materials International. 31 (2021) 165–179. https://doi.org/10.1016/j.pnsc.2021.01.007.

[21] M. Thommes, K. Kaneko, A.V. Neimark, J.P. Olivier, F. Rodriguez-Reinoso, J. Rouquerol, K.S.W. Sing, Physisorption of gases, with special reference to the evaluation of surface area and pore size distribution (IUPAC Technical Report), Pure Appl. Chem. 87 (2015) 1051–1069. https://doi.org/10.1515/pac-2014-1117.

[22] A.G. Slater, A.I. Cooper, Function-led design of new porous materials, Science. 348 (2015) aaa8075–aaa8075. https://doi.org/10.1126/science.aaa8075.

[23] P.E. de Jongh, P. Adelhelm, Nanoparticles and 3D Supported Nanomaterials, in: M. Hirscher (Ed.), Handbook of Hydrogen Storage, Wiley-VCH Verlag GmbH & Co. KGaA, Weinheim, Germany, 2010: pp. 279–340. https://doi.org/10.1002/9783527629800.ch10.

[24] S.L. Candelaria, Y. Shao, W. Zhou, X. Li, J. Xiao, J.-G. Zhang, Y. Wang, J. Liu, J. Li, G. Cao, Nanostructured carbon for energy storage and conversion, Nano Energy. 1 (2012) 195–220. https://doi.org/10.1016/j.nanoen.2011.11.006.

[25] R.B. Mathur, B.P. Singh, S. Pande, Carbon Nanomaterials: Synthesis, Structure, Properties and Applications, CRC Press, Taylor & Francis Group, Boca Raton, FL, USA, 2017.

[26] Vulcan XC-72 carbon black product data sheet, (n.d.).

[27] M.J. Lázaro, L. Calvillo, V. Celorrio, J. Pardo, S. Perathoner, R. Moliner, Study and application of Vulcan XC-72 in low temperature fuel cells, in: 2011: pp. 41–68.

[28] S. Sepp, Influence of porosity of the carbide-derived carbon on the properties of the composite electrocatalysts and characteristics of polymer electrolyte fuel cells, Dissertation, University of Tartu, 2017.

[29] A. Schneemann, J.L. White, S. Kang, S. Jeong, L.F. Wan, E.S. Cho, T.W. Heo, D. Prendergast, J.J. Urban, B.C. Wood, M.D. Allendorf, V. Stavila, Nanostructured Metal Hydrides for Hydrogen Storage, Chem. Rev. 118 (2018) 10775–10839. https://doi.org/10.1021/acs.chemrev.8b00313.

[30] E. Roduner, Size matters: why nanomaterials are different, Chem. Soc. Rev. 35 (2006) 583. https://doi.org/10.1039/b502142c.

[31] D.R. Lide, W.M.. Haynes, T.J. Bruno, eds., CRC Handbook of Chemistry and Physics, 97th Edition, 97th ed., CRC Press, 2017.

[32] S. Zheng, F. Fang, G. Zhou, G. Chen, L. Ouyang, M. Zhu, D. Sun, Hydrogen Storage Properties of Space-Confined $NaAlH_4$ Nanoparticles in Ordered Mesoporous Silica, Chemistry of Materials. 20 (2008) 3954–3958. https://doi.org/10.1021/cm8002063.

[33] C.P. Baldé, B.P.C. Hereijgers, J.H. Bitter, K.P. de Jong, Sodium Alanate Nanoparticles − Linking Size to Hydrogen Storage Properties, J. Am. Chem. Soc. 130 (2008) 6761–6765. https://doi.org/10.1021/ja710667v.

[34] K. Tuul, R. Palm, Influence of Nanoconfinement on the Hydrogen Release Processes from Sodium Alanate, Reactions. 2 (2021) 1–9. https://doi.org/10.3390/reactions2010001.

[35] R. Palm, H. Kurig, J. Aruväli, E. Lust, $NaAlH_4$/microporous carbon composite materials for reversible hydrogen storage, Microporous Mesoporous Mater. 264 (2018) 8–12. https://doi.org/10.1016/j.micromeso.2017.12.027.

[36] R.K. Bhakta, S. Maharrey, V. Stavila, A. Highley, T. Alam, E. Majzoub, M. Allendorf, Thermodynamics and kinetics of $NaAlH_4$ nanocluster decomposition, Phys. Chem. Chem. Phys. 14 (2012) 8160–8169. https://doi.org/10.1039/C2CP40196G.

[37] X. Liu, D. Peaslee, C.Z. Jost, E.H. Majzoub, Controlling the Decomposition Pathway of $LiBH_4$ via Confinement in Highly Ordered Nanoporous Carbon, J. Phys. Chem. C. 114 (2010) 14036–14041. https://doi.org/10.1021/jp1055045.

[38] P. Adelhelm, J. Gao, M.H.W. Verkuijlen, C. Rongeat, M. Herrich, P.J.M. van Bentum, O. Gutfleisch, A.P.M. Kentgens, K.P. de Jong, P.E. de Jongh, Comprehensive Study of Melt Infiltration for the Synthesis of $NaAlH_4$/C Nanocomposites, Chem. Mater. 22 (2010) 2233–2238. https://doi.org/10.1021/cm902681d.

[39] P.E. de Jongh, R.W.P. Wagemans, T.M. Eggenhuisen, B.S. Dauvillier, P.B. Radstake, Johannes.D. Meeldijk, J.W. Geus, K.P. de Jong, The Preparation of Carbon-Supported Magnesium Nanoparticles using Melt Infiltration, Chem. Mater. 19 (2007) 6052–6057. https://doi.org/10.1021/cm702205v.

[40] J. Gao, P. Adelhelm, M.H.W. Verkuijlen, C. Rongeat, M. Herrich, P.J.M. van Bentum, O. Gutfleisch, A.P.M. Kentgens, K.P. de Jong, P.E. de Jongh, Confinement of $NaAlH_4$ in Nanoporous Carbon: Impact on H_2 Release, Reversibility, and Thermodynamics, J. Phys. Chem. C. 114 (2010) 4675–4682. https://doi.org/10.1021/jp910511g.

[41] T. Mueller, G. Ceder, Effect of Particle Size on Hydrogen Release from Sodium Alanate Nanoparticles, ACS Nano. 4 (2010) 5647–5656. https://doi.org/10.1021/nn101224j.

[42] T.K. Nielsen, P. Javadian, M. Polanski, F. Besenbacher, J. Bystrzycki, T.R. Jensen, Nanoconfined $NaAlH_4$: Determination of Distinct Prolific Effects from Pore Size, Crystallite Size, and Surface Interactions, J. Phys. Chem. C. 116 (2012) 21046–21051. https://doi.org/10.1021/jp3049982.

[43] R. Palm, H. Kurig, J. Aruväli, E. Lust, $NaAlH_4$/microporous carbon composite materials for reversible hydrogen storage, Microporous and Mesoporous Materials. 264 (2018) 8–12. https://doi.org/10.1016/J.MICROMESO.2017.12.027.

[44] K. Tuul, $NaAlH_4$/Carbon Black Composite Materials for Hydrogen Storage, Bachelor's thesis, University of Tartu, 2019.

[45] R. Varin, T. Czujko, Z. s Wronski, Z. Zaranski, Nanomaterials for Hydrogen Storage Produced by Ball Milling, Canadian Metallurgical Quarterly. 48 (2009) 11–25. https://doi.org/10.1179/000844309794239143.

[46] D.L. Anton, Hydrogen desorption kinetics in transition metal modified NaAlH4, Journal of Alloys and Compounds. 356–357 (2003) 400–404. https://doi.org/10.1016/S0925-8388(03)00140-3.

[47] N.A. Ali, M. Ismail, Modification of $NaAlH_4$ properties using catalysts for solid-state hydrogen storage: A review, Int. J. Hydrogen Energy. (2020). https://doi.org/10.1016/j.ijhydene.2020.10.011.

[48] G. Sandrock, K. Gross, G. Thomas, Effect of Ti-catalyst content on the reversible hydrogen storage properties of the sodium alanates, J. Alloys Compd. 339 (2002) 299–308. https://doi.org/10.1016/S0925-8388(01)02014-X.

[49] K. Peinecke, M. Meggouh, M. Felderhoff, Mechanochemical synthesis and effect of various additives on the hydrogen absorption–desorption behavior of Na_3AlH_6, J Mater Sci. 53 (2018) 13742–13750. https://doi.org/10.1007/s10853-018-2279-3.

[50] M. Ismail, Study on the hydrogen storage properties and reaction mechanism of NaAlH4–MgH2–LiBH4 ternary-hydride system, Int. J. Hydrogen Energy. 39 (2014) 8340–8346. https://doi.org/10.1016/j.ijhydene.2014.03.166.

[51] L.L. Shaw, R. Ren, T. Markmaitree, W. Osborn, Effects of mechanical activation on dehydrogenation of the lithium amide and lithium hydride system, J. Alloys Compd. 448 (2008) 263–271. https://doi.org/10.1016/j.jallcom.2006.10.029.

[52] F.E. Pinkerton, Comparison of hydrogen cycling kinetics in $NaAlH_4$–carbon aerogel composites synthesized by melt infusion or ball milling, Journal of Alloys and Compounds. 509 (2011) 8958–8964. https://doi.org/10.1016/j.jallcom.2011.06.097.

[53] J. Huot, D.B. Ravnsbæk, J. Zhang, F. Cuevas, M. Latroche, T.R. Jensen, Mechanochemical synthesis of hydrogen storage materials, Progress in Materials Science. 58 (2013) 30–75. https://doi.org/10.1016/j.pmatsci.2012.07.001.

[54] C. Suryanarayana, Mechanical alloying and milling, Progress in Materials Science. 46 (2001) 1–184. https://doi.org/10.1016/S0079-6425(99)00010-9.

[55] Operating instructions for planetary mono mill PULVERISETTE 6 classic line, (2021).

[56] N. Hlabangana, G. Danha, E. Muzenda, Effect of ball and feed particle size distribution on the milling efficiency of a ball mill: An attainable region approach, South African Journal of Chemical Engineering. 25 (2018) 79–84. https://doi.org/10.1016/j.sajce.2018.02.001.

[57] A.I. Gusev, A.S. Kurlov, Production of nanocrystalline powders by high-energy ball milling: model and experiment, Nanotechnology. 19 (2008) 265302. https://doi.org/10.1088/0957-4484/19/26/265302.

[58] AutoChem 2950 HP Automated Catalyst Characterization System Operator's Manual, (2011).

[59] M.L. Huber, A.H. Harvey, Thermal Conductivity of Gases, in: CRC Handbook of Chemistry and Physics, CRC-Press, Boca Raton, FL, 2011: pp. 240–241. https://www.nist.gov/publications/thermal-conductivity-gases (accessed April 7, 2021).

[60] P. Atkins, J. De Paula, Atkins' Physical Chemistry, 8th ed., W. H. Freeman and Company, New York, NY, USA, 2006.

[61] S. Lowell, J.E. Shields, M.A. Thomas, M. Thommes, Characterization of Porous Solids and Powders: Surface Area, Pore Size and Density, Kluwer Academic Publishers, Dordrecht, the Netherlands, 2004.

[62] S. Brunauer, P.H. Emmett, E. Teller, Adsorption of Gases in Multimolecular Layers, J. Am. Chem. Soc. 60 (1938) 309–319. https://doi.org/10.1021/ja01269a023.

[63] D.D. Do, Adsorption Analysis: Equilibria and Kinetics, Imperial College Press, London, 1998.

[64] M. Thommes, K.A. Cychosz, Physical adsorption characterization of nanoporous materials: progress and challenges, Adsorption. 20 (2014) 233–250. https://doi.org/10.1007/s10450-014-9606-z.

[65] C. Suryanarayana, M.G. Norton, X-Ray Diffraction: A Practical Approach, Springer US, 1998. https://doi.org/10.1007/978-1-4899-0148-4.

[66] M. Ladd, R. Palmer, Crystal Morphology and Crystal Symmetry, in: M. Ladd, R. Palmer (Eds.), Structure Determination by X-Ray Crystallography: Analysis by X-Rays and Neutrons, Springer US, Boston, MA, 2013: pp. 1–50. https://doi.org/10.1007/978-1-4614-3954-7_1.

[67] W.H. Bragg, W.L. Bragg, The reflection of X-rays by crystals, Proc. R. Soc. Lond. A. 88 (1913) 428–438. https://doi.org/10.1098/rspa.1913.0040.

[68] M. Ladd, R. Palmer, Powder Diffraction, in: M. Ladd, R. Palmer (Eds.), Structure Determination by X-Ray Crystallography: Analysis by X-Rays and Neutrons, Springer US, Boston, MA, 2013: pp. 585–634. https://doi.org/10.1007/978-1-4614-3954-7_12.

[69] iSorb HP series High Pressure Gas Sorption System Operating Manual, (2019).

[70] S. Gates-Rector, T. Blanton, The Powder Diffraction File: a quality materials characterization database, Powder Diffraction. 34 (2019) 352–360. https://doi.org/10.1017/S0885715619000812.

Kuulveskis jahvatatud $NaAlH_4$/süsiniktahm komposiitmaterjalid vesiniku pöörduvaks salvestamiseks

Leidmaks uusi tõhusamaid ja majanduslikult tasuvamaid lahendusi taastuvatest energiaallikatest toodetud vesiniku salvestamiseks on tarvis arendada välja uut salvestustehnoloogiat suuremate energiatiheduste saavutamiseks. Ühe potentsiaalse vesinikku salvestava süsteemina sünteesiti kuuljahvatamise meetodil naatriumalaumiiniumhüdriidi ($NaAlH_4$) ja mesopoorse süsiniktahma Vulcan XC72R põhjal komposiitmaterjalid. Nendes materjalides oli kõrge $NaAlH_4$ massiprotsendiline sisaldus ning neid karakteriseeriti eesmärgiga hinnata nende sobivust vesinikku pöörduvalt salvestavaks materjaliks. Selleks kasutati temperatuur-programmeeritud dehüdrogeenimise, gaasi sorptsiooni, röntgendifraktsioonanalüüsi ja dehüdrogeenimise/hüdrogeenimise tsükleerimise meetodeid.

Tulemustest selgus, et kuuljahvatamise, süsiniku kasutamise ja $NaAlH_4$ nanoosakeste kujule viimine avaldas head mõju materjali vesiniku eraldamise omadustele. Erinevalt puistematerjalist, eraldus mingi hulk vesinikku lausa toatingimustel ning intensiivsem eraldumine toimus temperatuuridel alates 100 °C. Orientiiriks praktiliste rakenduste jaoks on PEM kütuseelemendi töötemperatuur, mis jääb alla 80 °C. Tsükleerimisel leiti, et materjali on võimalik vesinikku täis laadida juba 150 °C ja 60 bar H_2 rõhu juures. Siiski selgus, et materjali vesiniku salvestamise võime kahaneb tsükleerimise tulemusel. Selle põhjuseks oli eeldatavasti laguproduktide ruumiline eraldatus, hüdriidide aglomereerumine suuremateks osakesteks ning suuremate osakeste laadimise kineetiline piiratus. Siiski tuleb tõdeda, et väga lihtsa ja paindliku sünteesimeetodiga saavutati muljetavaldavad tulemused. Täiendavalt tuleks optimeerida sünteesiparameetreid, süsiniku valikut ning vahest kaasata ka katalüsaatoreid, et langetada materjali vesiniku eraldumise temperatuuri ning laadimise temperatuuri ja rõhku veelgi.

ACKNOWLEDGEMENTS

This work was supported by the EU through the European Regional Development Fund under project TK141 2014-2020.4.01.15-0011 and Estonian Research Council grant PRG676.

I would first and foremost like to thank my supervisor, Dr. Rasmus Palm, for his guidance and support. There would be no thesis without him. I am also very grateful to Prof. Enn Lust and the Laboratory of Physical Chemistry for providing the conditions and opportunity to conduct research and develop myself. I would also like to extend my gratitude towards Mr. Jaan Aruväli and Prof. Kalle Kirsimäe from the Geology department for the XRD measurements.

I am most grateful for all of my friends, coursemates, and colleagues who have helped and supported me both actively and passively. I am immensely appreciative of office 5071, a great crowd who've made this place somewhere I belong. Special thanks to the future Canadian Anu. You'll leave behind a void far more significant than a simple office space. I want to extend my thanks and kind words to Dr. Ove Korjus, who has not only always helped out, even when not asked, but also has entertained interesting discussions about X-ray diffraction and mental health (semi-related topics). I am very proud of Mr. Egert Möller for being an excellent student. I would also like to acknowledge Mr. Rait Kanarbik for keeping the Institute of Chemistry up and running and being the hero we need during our darkest hours.

Finally, it is difficult to fully express my love and appreciation for Kertu, who has seen me through all of the ups and downs of the past two years (and the two and a half before those).

From the bottom of my heart to all those, named and unnamed, that find themselves in these acknowledgments: life is an adventure, and I am glad that you've stuck around with me so far. Stay tuned for our next episode – the PhD.

SUPPLEMENTARY INFORMATION

Supplementary Section 1. Schematic of the AutoChem 2950 HP chemisorption analyzer.

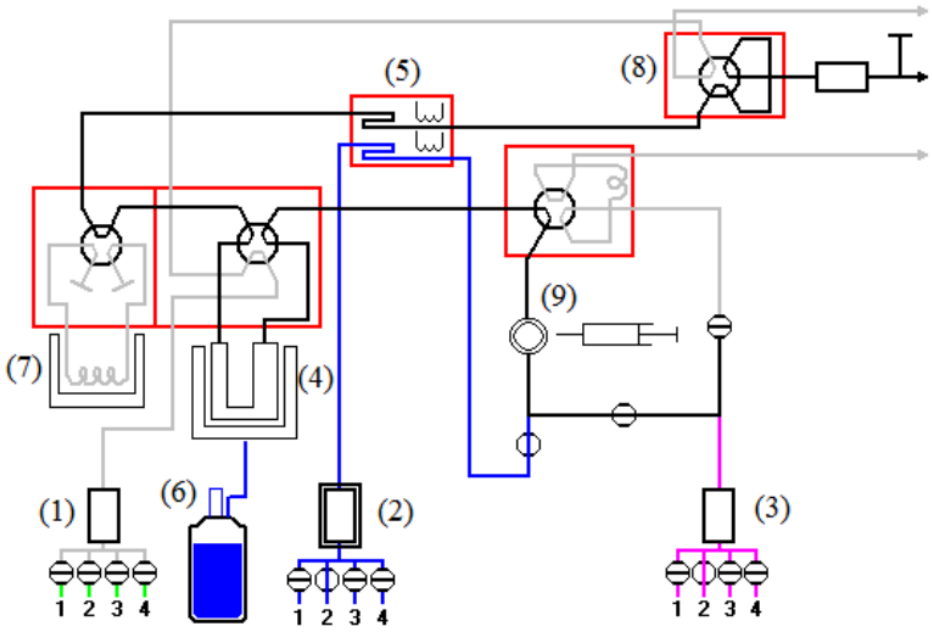

Supplementary Figure 1. Schematic of the AutoChem 2950 HP chemisorption analyzer. (1) input for preparation gas, (2) input for carrier gas, (3) input for analysis gas, (4) sample cell and furnace, (5) thermal conductivity detector, (6) coolant pump, (7) condenser, (8) mass flow controller, (9) septum for manual dosing. Schematic based on previous work by Dr. R. Palm.

Supplementary Section 2. Gas sorption data.

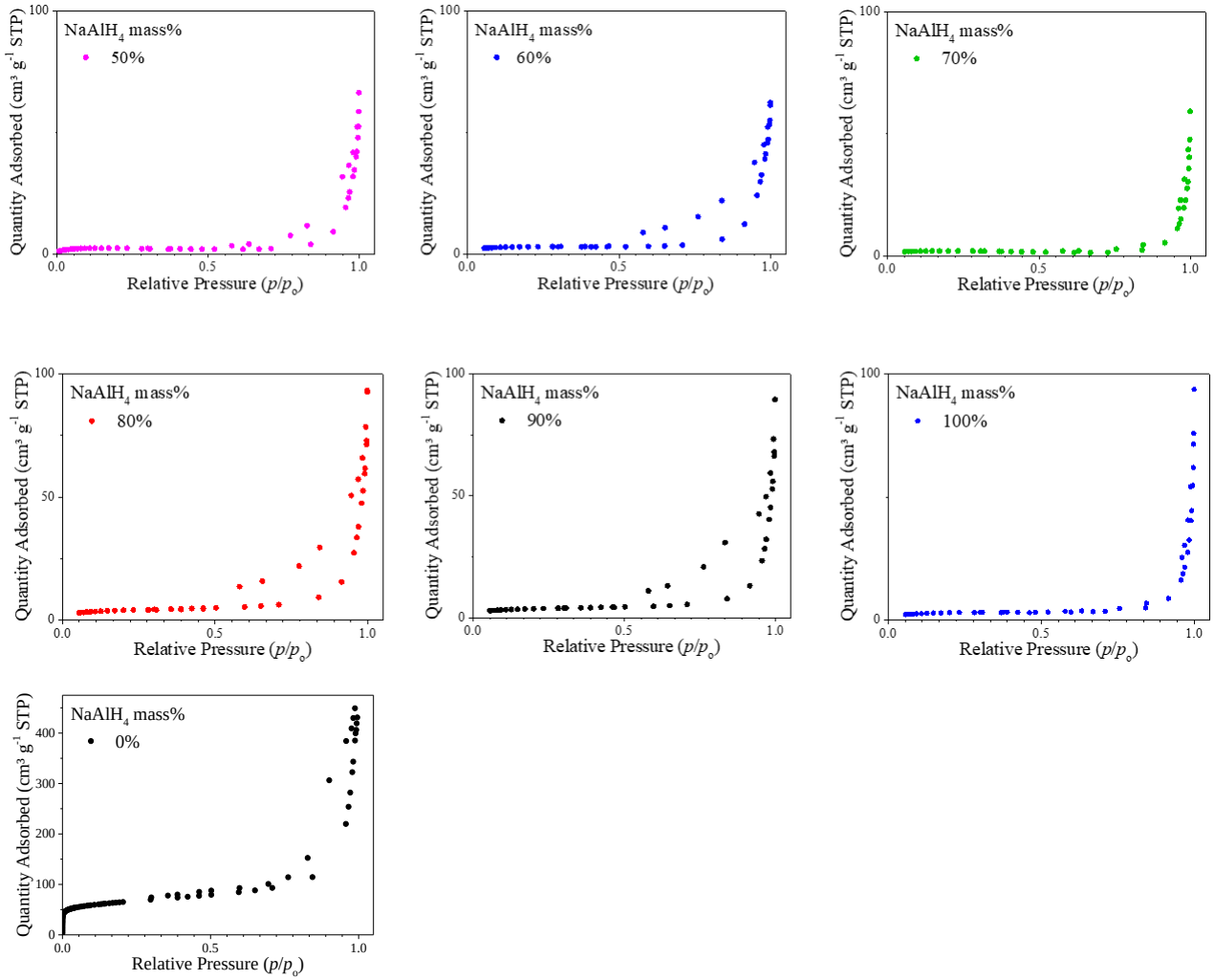

Supplementary Figure 2. N_2 isotherms of ball-milled $NaAlH_4$, ball-milled Vulcan XC72R, and $NaAlH_4$/Vulcan XC72R composites.

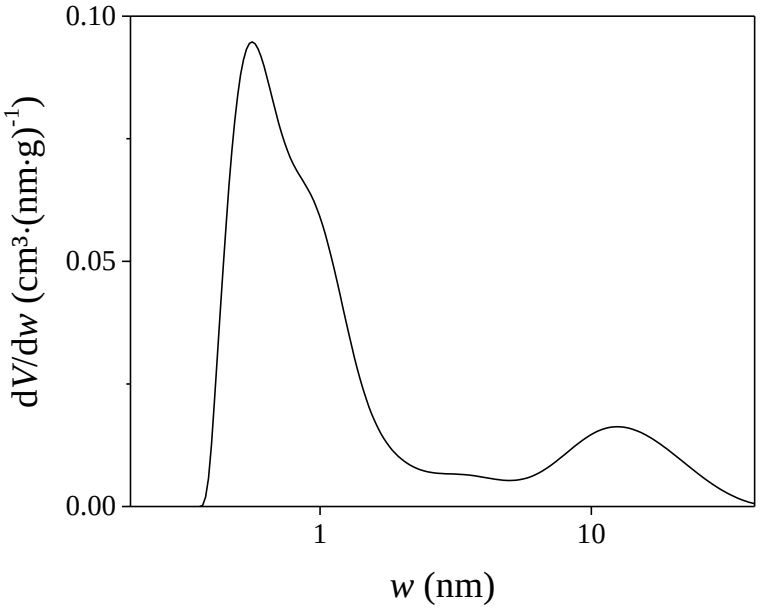

Supplementary Figure 3. Ball-milled Vulcan XC72R differential pore size distribution calculated from N_2 isotherm using the SAIEUS software and 2D-NLDFT-HS model[1].

[1] J. Jagiello, J.P. Olivier, 2D-NLDFT adsorption models for carbon slit-shaped pores with surface energetical heterogeneity and geometrical corrugation, Carbon. 55 (2013) 70–80. https://doi.org/10.1016/j.carbon.2012.12.011.

Supplementary Section 3. Results of the cycling experiments: time dependence of H_2 evolution.

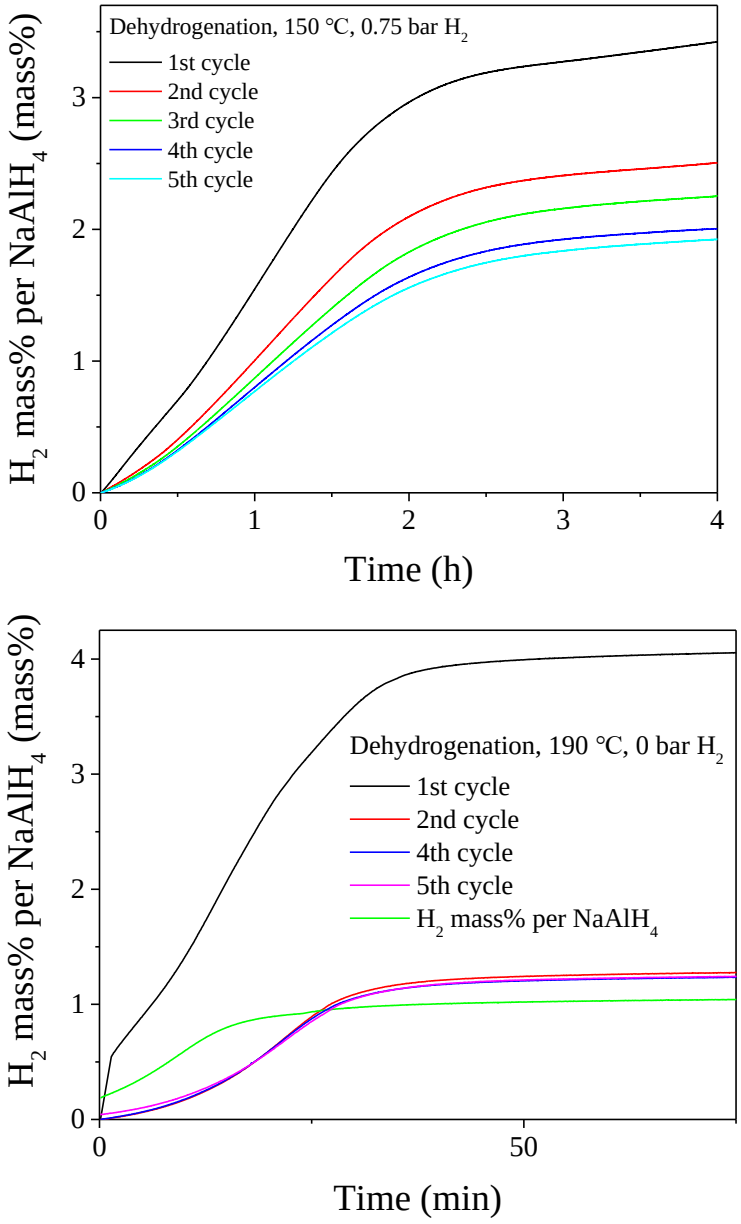

Supplementary Figure 4. Time dependence of evolved hydrogen during cycling experiments. First 5 cycles presented for 150 °C cycling. 3rd cycle of 190 °C cycling is deviant due to technical issues.

Non-exclusive licence to reproduce thesis and make thesis public

I, Kenneth Tuul,

1. herewith grant the University of Tartu a free permit (non-exclusive licence) to:

1.1. reproduce, for the purpose of preservation, including for adding to the DSpace digital archives until the expiry of the term of copyright, and

1.2. make available to the public via the web environment of the University of Tartu, including via the DSpace digital archives, under the Creative Commons licence CC BY NC ND 3.0, which allows, by giving appropriate credit to the author, to reproduce, distribute the work and communicate it to the public, and prohibits the creation of derivative works and any commercial use of the work from ***30/06/2023*** until the expiry of the term of copyright,

"Ball-milled $NaAlH_4$/carbon black composites for reversible hydrogen storage",

supervised by Dr. Rasmus Palm,

2. I am aware of the fact that the author retains the rights specified in p. 1.

3. I certify that granting the non-exclusive licence does not infringe other persons' intellectual property rights or rights arising from the personal data protection legislation.

Kenneth Tuul

05/06/2021